Effects of Extrinsic and Intrinsic Proton Activity on The Mechanism of Oxygen Reduction in Ionic Liquids

by

Robert August Zeller

A Dissertation Presented in Partial Fulfillment
of the Requirements for the Degree
Doctor of Philosophy

Approved November 2011 by the
Graduate Supervisory Committee:

Cody Friesen, Chair
Karl Sieradzki
Daniel Buttry

ARIZONA STATE UNIVERSITY

December 2011

ABSTRACT

Mechanisms for oxygen reduction are proposed for three distinct cases covering two ionic liquids of fundamentally different archetypes and almost thirty orders of magnitude of proton activity. Proton activity is treated both extrinsically by varying the concentration and intrinsically by selecting proton donors with a wide range of aqueous pK_a values.

The mechanism of oxygen reduction in ionic liquids is introduced by way of the protic ionic liquid (pIL) triethylammonium triflate (TEATf) which shares some similarities with aqueous acid solutions. Oxygen reduction in TEATf begins as the one electron rate limited step to form superoxide, $O_2^{\bullet -}$, which is then rapidly protonated by the pIL cation forming the perhydroxyl radical, $HO_2^{\bullet}$. The perhydroxyl radical is further reduced to peroxidate (HO_2^-) and hydrogen peroxide in proportions in accordance with their pK_a. The reaction does not proceed beyond this point due to the adsorption of the conjugate base triethylammine interfering with the disproportionation of hydrogen peroxide. This work demonstrates that this mechanism is consistent across Pt, Au, Pd, and Ag electrodes.

Two related sets of experiments were performed in the inherently aprotic ionic liquid 1-butyl-2,3-dimethylimidazolium triflate (C_4dMImTf). The first involved the titration of acidic species of varying aqueous pK_a into the IL while monitoring the extent of oxygen reduction as a function of pK_a and potential on Pt and glassy carbon (GC) electrodes. These experiments confirmed the greater propensity of Pt to reduce oxygen by its immediate and abrupt transition from one electron reduction to four electron reduction, while oxygen reduction on GC gradually approaches four electron reduction as the potentials were driven more cathodic. The potential at which oxygen reduction initiates shows general agreement with the Nernst equa-

tion and the acid's tabulated aqueous pK_a value, however at the extremely acidic end, a small deviation is observed.

The second set of experiments in C_4dMImTf solicited water as the proton donor for oxygen reduction in an approximation of the aqueous alkaline case. The water content was varied between extremely dry (< 0.1mol% H_2O) and saturated (approximately 15.8mol% H_2O). As the water content increased so too did the extent of oxygen reduction eventually approach two electrons on both Pt and GC. However, additional water led to a linear increase in the Tafel slope under enhanced mass transport conditions up to the point of 10mol% water. This inhibition of oxygen adsorption is the result of the interaction between superoxide and water and more specifically is proposed to be associated with decomposition of the C_4dMIm^+ cation by hydroxide at the elevated temperatures required for the experiment. Oxygen reduction on both Pt and GC follows Nernstian behavior as the water content is increased. Separate mechanisms for oxygen reduction on Pt and GC are proposed based on the nature of the Nernstian response in these systems.

ACKNOWLEDGEMENTS

First and foremost, I am indebted to Dr. Elise Switzer for her help in learning the rotating ring-disk electrode techniques, development of a stable psuedo reference electrode, and complimentary experiments that help provide a full picture for the protic additive work presented in Chapter 3. Without her assistance this part of the project would have taken months longer to complete and I would have missed many other exciting opportunities related to my original motivation for attending a Ph.D. program.

I also owe my gratitude to Dr. Lei Tang and Dr. Jose Bautista-Martinez who introduced me to the science of ionic liquids and oxygen reduction. My experience in interpreting their work and providing supporting experiments was an excellent foundation from which to design and pursue this project. Dr. Tang has generously permitted me to include many of her experiments on oxygen reduction in protic ionic liquids in this document as an introduction to these exotic solvents.

I would also like to thank Fluidic Energy for the synthesis and donation of many exceptionally pure aprotic ionic liquids. That company's generosity enabled this project to take on the ambitious scale it did.

Finally, I would like to acknowledge Janice Kyle and Christine Roeger of the ASU Glassblowing Facility for their consultation in designing many of the electrochemical cells and other apparatus that made this project possible. Ionic liquids are expensive to purchase and time intensive to synthesize, and their skill permitted the construction of jacketed RRDE cells with remarkably small working volumes that economized even our generous supply.

TABLE OF CONTENTS

LIST OF TABLES

LIST OF FIGURES

Chapter 1

INTRODUCTION

Oxygen is an abundant and reactive element comprising almost 21vol% of the earth's atmosphere. It is also electrochemically reducible and thus the electrochemical energy released during the reaction of oxygen with less noble species can be collected and exploited, much like the heat of combustion in a fire. However, a fundamental advantage of electrochemical energy is the direct conversion of chemical potential into electricity, bypassing any need for moving parts or the limitations of Carnot efficiency. This is the advantage of the energy produced by fuel cells and air-batteries.

All devices that exploit the oxygen reduction reaction share a fundamental challenge that limits their market acceptance: evaporation. Air-batteries and fuel cells must be open to the atmosphere in order collect and reduce atmospheric oxygen and this permits the evaporation of their electrolyte. Hydrogen fuel cells typically use Nafion® membranes as their electrolyte and produce water during the reduction of oxygen. The conductivity of the membrane and hence performance is strongly influenced by the relative humidity of their environment [1]. In air-batteries, particularly the alkaline Zn-air cell, the evaporation of the electrolyte frequently leads to premature cell death or absorption of atmospheric moisture leading to flooding of the air cathode [2].

In addition to the practical problems of managing water within an open cell, aqueous chemistries are also limited by the electrochemical stability of water. Anode materials less nobel than Zn, and therefore more energetic, have proven too reactive in aqueous solutions to be commercially viable. In fact, corrosion of Zn via hydrogen evolution from the spontaneous reduction of the electrolyte is a persistent

problem in current alkaline Zn-air cells. This places a fundamental limitation on both the long term stability and specific energy of the battery fuel.

Room temperature ionic liquids (ILs) are a relatively new class of solvent which are poised to solve both the evaporation and electrochemical stability challenges. Ionic liquids have wide electrochemical windows, commonly exceeding 2.5V [3] and negligible vapor pressures [4; 5]. Ionic liquids obtain these properties because they are composed of large stable organic cations generally paired with similarly large organic anions. The large diffuse charges on asymmetric cations keeps many of these salts liquid at room temperature and below. Being ionic, ILs are also inherently conductive and no separate salts are required to produce an electrolyte.

Ideally, the ionic liquids used in an electrochemical energy device do not undergo faradaic reactions within the electrochemical window of the device. Unfortunately, inert aprotic solvents are typically poor candidates for supporting oxygen reduction as the process cannot proceed beyond the formation of the superoxide species ($O_2^{\bullet -}$) without some acid source, be it Lewis or Brönsted in nature [6]. This dissertation will outline the mechanism of oxygen reduction in three different cases analogous to oxygen reduction in aqueous acid and aqueous alkaline conditions.

First, by way of introduction to the electrochemical techniques and the electrochemical behavior of ionic liquids, the oxygen reduction mechanism in the inherently protic ionic liquid (pIL) triethylammonium triflate (TEATf) is developed. This ionic liquid is analogous to a weakly acidic aqueous solution in that there are protons readily available to protonate the reduced oxygen. The effective pH of this class of ionic liquids is also well understood [7].

Second, a variety of Brönsted acid species have been titrated into the otherwise aprotic ionic liquid 1-butyl-2,3-dimethylimidazolium triflate (C_4dMImTf) and the

progress of oxygen reduction tracked with respect to acid pK_a and potential. By carefully selecting the the host ionic liquid it was possible to examine almost thirty orders of magnitude of proton activity.

Finally, water was used as the proton source in C_4dMImTf and the extent of oxygen reduction obtainable was evaluated. This case proved more complicated than originally anticipated due to the complex interaction between water and the ionic liquid anion. Increasing water content appears to inhibit the formation of superoxide by restricting the adsorption of O_2 while simultaneously protonating the superoxide to form the peroxidate species, $HO_2^{\bullet -}$. A tentative explanation for how both phenomena can occur is advanced.

Chapter 2

BACKGROUND

2.1 Oxygen Reduction Fundamentals

Oxygen reduction in aqueous systems has been heavily studied for decades, and many high quality reviews exist [8–11]. These tend to focus on the mechanisms of ORR as a function of pH [12–15] or on the selection and construction of catalysts [16–18]. In aqueous solutions, platinum and its alloys are reliably the best ORR catalysts across all pH ranges [11; 19; 20], with Au performing equally well in some limited circumstances [17; 21; 22].

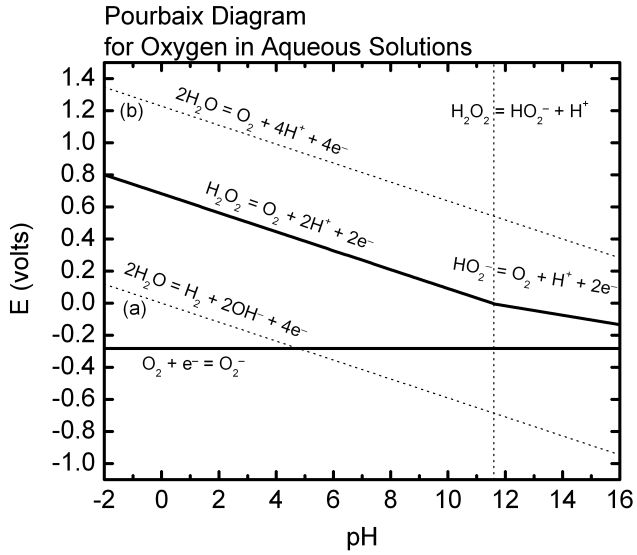

Figure 2.1: Pourbaix diagram of selected oxygen species in aqueous solutions. Shows the equilibrium species as a function of pH and electrochemical potential at standard state. Plotted from data in reference [23].

Figure 2.1 is a Pourbaix diagram, a kind of phase diagram in potential-pH space, for some selected oxygen species in aqueous solutions. Lines (a) and (b) define the thermodynamic stability limits of water. At potentials less than those defined

by line (a) water is reduced to form hydrogen gas at a pressure of 1 atm, while at potentials above line (b) it is oxidized to form oxygen. Within the stability limits of water, hydrogen peroxide is stable. Also shown is the pH independent formation of the superoxide species ($O_2^{\bullet -}$) and the pH of 11.7, at which protons are removed from hydrogen peroxide to form the peroxidate anion. Reaction 2.1 is plotted as a bold line between lines (a) and (b).

$$O_2 + 2H^+ + 2e^- \leftrightarrow H_2O_2 \tag{2.1}$$

$$\begin{aligned} E &= E^o_{H_2O_2} + \frac{RT}{nF} \ln \frac{[H_2O_2]}{[H^+]^2 \cdot P_{O_2}} \\ E &= 0.682 - 0.0591 pH + 0.0295 \log \frac{[H_2O_2]}{P_{O_2}} \end{aligned} \tag{2.2}$$

By writing the free energy of Rxn. 2.1 in terms of the electrochemical potential through $\Delta G^o = -nF\Delta E^o = -RT \ln K$ a relationship between the partial pressure of oxygen, concentration of H_2O_2 and pH is derived as Eqn. 2.2. It is this variation in potential with respect to pH that is plotted as a bold line in Fig. 2.1 for $\log\left(\frac{[H_2O_2]}{P_{O_2}}\right) = 0$.

Equation 2.2, in its simplified form, clearly shows a decrease in the oxygen reduction potential of approximately 60mV with every ten-fold decrease in proton activity. Through the Henderson-Hasselbalch equation (Eqn. 2.3) the pH used to build the Pourbaix diagram is related to the strength of a generic acid, HA, through its pK_a.

$$pH = pK_a^{HA} + \log \frac{[A^-]}{[HA]} \tag{2.3}$$

It is now possible to rewrite Eqn. 2.2 more generally for acids in any solvent.

$$O_2 + 2HA + 2e^- \leftrightarrow H_2O_2 + 2A^- \tag{2.4}$$

$$\begin{aligned} E &= E^o_{H_2O_2} - \frac{RT}{nF}\ln\frac{[H_2O_2][A^-]^2}{[HA]^2 \cdot P_{O_2}} \\ &= E^o_{H_2O_2} - \frac{2RT}{nF}\ln\frac{[H^+][A^-]}{[HA]} - \frac{RT}{nF}\ln\frac{[H_2O_2]}{[H^+]^2 \cdot P_{O_2}} \\ &= E^o_{H_2O_2} - \frac{2RT}{nF}(pH - pK_a) - \frac{RT}{nF}\ln\frac{[H_2O_2]}{P_{O_2}} \\ &= 0.682 - 0.0591(pH - pK_a) - 0.0295\log\frac{[H_2O_2]}{P_{O_2}} \end{aligned} \tag{2.5}$$

After simplifying and evaluating some of the terms in Eqn. 2.5 it becomes apparent that decreasing the pK_a of a proton donor has the same impact as making the solution more acidic, i.e. stronger proton donors drive Rxn. 2.4 to the right and raise the potential of oxygen reduction. In the final forms of Eqn. 2.5 the equivalent contributions to the oxygen reduction potential are explicitly separated into the proton binding energy, represented by pK_a, and proton concentration (pH).

ORR Mechanism in Aqueous Alkaline

In aqueous alkaline electrolytes, absent strongly adsorbing species, the mechanism of four-electron oxygen reduction on platinum engenders some uncertainty [11; 24], though there is consensus on the initial stages. Upon adsorption of O_2, the mechanism starts with a single electron transfer to the dioxygen molecule to produce superoxide, which is then rapidly protonated by water.

$$O_2(ads) + e^- \rightarrow O_2^{\bullet -}(ads) \tag{2.6}$$

$$O_2^{\bullet -}(ads) + H_2O \rightarrow HO_2^{(\bullet/-)}(ads) + OH^{(-/\bullet)} \tag{2.7}$$

From here, authors diverge in their proposed mechanisms. Ross [11] prefers a mechanism which involves the intermediate formation of adsorbed atomic oxygen

and the spontaneous and rapid disproportionation of peroxidate.

$$O_2(ads) + e^- \rightarrow O_2^{\bullet -}(ads)$$
$$O_2^{\bullet -}(ads) + H_2O \rightarrow HO_2^{(\bullet/-)}(ads) + OH^{(-/\bullet)}$$
$$HO_2^{(\bullet/-)} \rightarrow O(ads) + OH^{(\bullet/-)}(ads) \quad (2.8)$$
$$O(ads) + H_2O + e^- \rightarrow OH^{\bullet}(ads) + OH^- \quad (2.9)$$
$$2OH^{\bullet} + 2e^- \rightarrow 2OH^- \quad (2.10)$$

Durand [24], on the other hand, proposes a mixture of two mechanisms depending on the roughness of the Pt surface. On smooth single crystal platinum, Durand claims that the primary ORR mechanism bypasses formation of peroxidate, instead favoring proton driven cleavage of the oxygen-oxygen bond.

$$O_2(ads) + e^- \rightarrow O_2^{\bullet -}(ads)$$
$$O_2^{\bullet -}(ads) + H_2O \rightarrow HO_2^{\bullet}(ads) + OH^-$$
$$HO_2^{\bullet}(ads) + H_2O \rightarrow 3OH^{\bullet}(ads) \quad (2.11)$$
$$3OH^{\bullet}(ads) + 3e^- \rightarrow 3OH^- \quad (2.12)$$

On small Pt particles, fine grain polycrystals, or mechanically polished surfaces, Durand finds some evidence for a two electron peroxidate pathway:

$$O_2(ads) + e^- \rightarrow O_2^{\bullet -}(ads)$$
$$O_2^{\bullet -}(ads) + H_2O \rightarrow HO_2^{\bullet}(ads) + OH^-$$
$$HO_2^{\bullet}(ads) + e^- \rightarrow HO_2^-(ads) \quad (2.13)$$
$$2HO_2^-(ads) \rightarrow O_2 + 2OH^-. \quad (2.14)$$

All of these mechanisms result in the accepted net reaction of:

$$O_2 + 2H_2O + 4e^- \rightarrow 4OH^-. \quad (2.15)$$

ORR Mechanism in Aqueous Acids

In acidic media, the availability of free protons simplifies the mechanism as hydronium is consumed instead of water. This results in the rapid protonation of peroxidate to form hydrogen peroxide.

$$\begin{aligned} O_2(ads) + e^- &\rightarrow O_2^{\bullet -}(ads) \\ O_2^{\bullet -}(ads) + H^+ &\rightarrow HO_2^{\bullet}(ads) \\ HO_2^{\bullet}(ads) + e^- &\rightarrow HO_2^-(ads) \\ HO_2^-(ads) + H^+ &\rightarrow H_2O_2 \end{aligned} \tag{2.16}$$

For a net reaction of:

$$O_2 + 2H^+ + 2e^- \rightarrow H_2O_2. \tag{2.17}$$

Hydrogen peroxide can decompose either chemically or electrochemically to complete the four electron reduction [23; 25–29].

$$2H_2O_2 \rightarrow O_2 + 2H_2O \tag{2.18}$$

or

$$H_2O_2 + e^- \rightarrow OH^- + OH^{\bullet}(ads) \tag{2.19}$$

$$OH^{\bullet}(ads) + e^- \rightarrow OH^-$$

$$2OH^- + 2H^+ \rightarrow 2H_2O \tag{2.20}$$

On platinum surfaces, the under potential deposition of hydrogen inhibits the adsorption and consequent electrochemical reduction of hydrogen peroxide at high overpotentials [20], while at low overpotentials hydroxyl adsorption prevents its disproportionation [30; 31].

Oxygen Reduction in Non-aqueous Media

With the mechanism of ORR so closely tied to the coverage of the surface by $OH^{\bullet}(ads)$ and availability of protons, either from an acid source or the deprotonation of water, some investigations have pursued oxygen reduction in aprotic solvents such as dimethylformamide (DMF), dimethyl sulfoxide (DMSO), and acetonitrile (ACN) [6; 32–37]. The findings of these studies have revealed some interesting complexities in the ORR mechanism. Across a broad range of solvents and catalysts, the rate limiting step in ORR is usually the injection of the first electron to form superoxide [11]. In aprotic solvents this is a readily reversible process, but it becomes irreversible with the small addition of weakly acidic species such as phenol ($pK_a = 10$) [6; 36–39].

The proton transfer from phenol to superoxide is surprising given the perhydroxyl radical's relatively low pK_a of ca. 4.7 in aqueous [34; 40]. However its conjugate base is able to drive the net reaction

$$2O_2^{\bullet -} + H_2O \rightarrow O_2 + HO_2^- + OH^-, \quad K = 0.91 \cdot 10^9 \tag{2.21}$$

so completely that it behaves as though it has a proton affinity similar to $pK_a = 24$ [34]. The same author estimates the pK_a of $HO2^{\bullet}$ in DMF as ca. 12 due to the much weaker solvation in non-aqueous solvents [6].

Dry solutions cannot follow the aqueous alkaline four electron reduction mechanism regardless of proton concentration because unlike hydroxyl, the conjugate base of the proton donor is not reducible. Therefore, above some pK_a one would only expect to see two electron reduction. This pK_a is likely related closely to the deactivation of this proton transfer: $H_2O_2 + 2e^- + 2H^+ \rightarrow 2H_2O$ [23].

At least two studies have examined the protonation of superoxide by phenol-related compounds in ionic liquids [38; 39] and both found evidence for two electron reduction on gold and glassy carbon electrodes. Unfortunately both studies used imidazolium based cations with the C2 proton intact which is sufficiently acidic to irreversibly protonate superoxide (see Section 2.5). Further, both ILs used the Tf_2N cation which was found to be unstable in the presence of phenolate [38].

2.2 Ionic Liquids

Ionic liquids (ILs) are a relatively new class of solvents composed primarily of large organic ions [3]. Their individual physical and chemical properties can vary over a broad range, but in general an ionic liquid is suitable for electrochemistry when it has a low melting point ($T_m < 100°C$), moderate specific conductivity, and a wide electrochemical window [41]. Due to their ionic nature and large molar mass, ILs reliably low vapor pressures [4; 5]. They also have low molar densities which makes their physicochemical properties especially sensitive to impurities or additives.

Ionic liquids have been classified under a variety of schemes and generations. Most useful among these distinctions are whether or not they (i) are stable in the presence of moist air, (ii) contain electrochemically accessible protons, and (iii) are miscible with water. Early first generation ionic liquids were formed by the transfer of a halide from an organic salt to a very strong Lewis acid, such as $AlCl_3$. The reactivity of the resulting $AlCl_4^-$ anion made the ILs unstable in the presence of air or water.

Table 2.1 lists physicochemical properties relevant to ORR for a selection of common electrochemical solvents and ionic liquids. The ionic liquids in the table represent three common cations: a dialkylpyrrolidinium (C_4nmp), dialkylimidazolium

Solvent	C_{O_2} mM	$D_{O_2} \cdot 10^6$ $cm^2 s^{-1}$	Viscosity $mPa \cdot s$	Density $g \cdot cm^{-3}$	Method	Ref.
water	1.26	$19-20$			Van Slyke	[42]
	1.24	24.2	0.890	0.997		[43]
0.1M KCl	1.18	21.2	0.890	1.006	Winkler	[44]
0.5M H_2SO_4	1.22	10.4			μPt	[45]
	1.16	13.4			μAu	[45]
DMF	4.72 ± 0.1	47.6 ± 2.4	0.8473[a]		RDE CC	[46]
	4.5 ± 0.3	47			GC	[47]
		45.8 ± 0.31			RDE	[35]
		53.5 ± 0.35			CV	[35]
			0.794	0.944		[43]
DMSO	2.24 ± 0.1	20.8 ± 2.7	2.087[a]		RDE CC	[46]
	2.1 ± 0.1				GC	[47]
		30.5 ± 3.5			RDE	[35]
		31.1 ± 0.9			CV	[35]
			1.987	1.101		[43]
Acetonitrile	8.21 ± 0.6	71.2 ± 6.4	0.356[a]		RDE CC	[46]
	8.1 ± 0.6				GC	[47]
		70.3 ± 4.5			RDE	[35]
		70.5 ± 5.3			CV	[35]
			0.369	0.786		[43]
C_4nmpTf_2N	3.6	5.49			μAu	[48]
	6.1 ± 0.8	5.2 ± 0.4			μAu / μPt	[49]
	13.6 ± 0.8	1.8 ± 0.2	89		μAu	[50]
			85	1.41	Ostwald	[51]
			~ 75	1.40	Stabinger	[52]
			76		Rolling-ball	[53]
C_4dmimTf_2N	3.6	5.05			μAu	[48]
	7.2 ± 0.8	2.1			μAu	[54]
	5.34 ± 0.1	3.90 ± 0.07			μPt	[55]
			88		Rolling-ball	[53]
				1.453[b]		
C_4mimTf_2N	3.1	8.76			μAu	[48]
		6.1			SECM	[56]
			47		Rolling-ball	[53]
			52	1.429		[57]
C_4mimTf	$2.2-4.7$[b]	$4.53-8.57$[b]		1.29[b]	μPt	
			~ 75	1.3	Stabinger	[52]
			83.2			[58]
			90	1.290		[57]

Table 2.1: O_2 physicochemical properties in selected solvents and aprotic ionic liquids near 25°C.

[a] calculated using density from the CRC: Handbook of Chemistry and Physics [43]

[b] not available in literature

(C_4MIm), and a C2 substituted dialkylimidazolium (C_4dMIm). Paired with these are two of the most common air stable anions: bis(trifluoromethanesulfonyl)imide (Tf_2N) and trifluoromethanesulfonate (triflate, Tf).

With a broad selection of ions, the ability to tune water solubility, and the decoupling of proton activity from concentration, ionic liquids may have the potential to enhance the ORR capabilities of less expensive catalysts.

Protic vs Aprotic Ionic Liquids

Among air stable ILs, a subclass are formed simply by proton transfer between a Brönsted acid, HA, and a Brönsted base, B: $HA + B \rightarrow A^- + BH^+$. The difference in pK_a between a proton residing on the acid, pK_a^{HA}, and a proton captured by the base, $pK_a^{BH^+}$, determines many of the properties of the protic ionic liquid (pIL). Larger differences in pK_a's ($\Delta pK_a = pK_a^{BH^+} - pK_a^{HA}$) generally result in ILs with lower vapor pressure, wider electrochemical windows, and higher melting points [7; 59; 60].

Fig. 2.2 shows a cyclic voltammagram on Pt in the pIL triethylammonium triflate (TEATf), formed by the temperature controlled equimolar mixture of triethylamine with triflic acid. Like water, the cathodic stability limit of the pIL is associated with the reversible reduction of H^+ to H_2. In this case supported by the ammonium cation and the resultant neutral amine [7]. However the anodic stability limit is approximately 2.5V more anodic and set by the oxidative stability of the triflate anion. Platinum oxidizes before this point, as visible in the slow oxidation wave beginning at 1V vs Pd/H, and the corresponding reduction wave below 1.0V. The small oxidation wave above 0V vs Pd/H is the oxidation of residual hydrogen gas to form triflic acid [7].

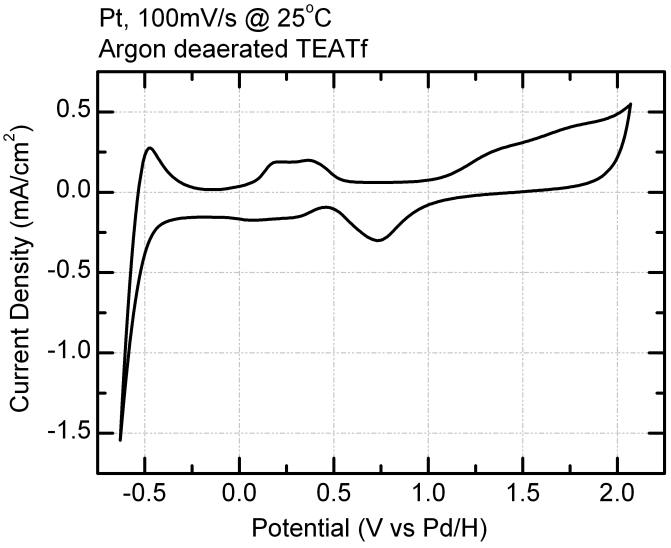

Figure 2.2: Cyclic voltammagram on Pt in argon deaerated TEATf at 100mV/s. Data replotted from reference [61].

Aprotic ILs in contrast, are generally formed by alkylation where an alkyl chain is transferred to form a cation instead of a proton. Following alkylation, the anion of the resulting pair can be exchanged to the anion of interest through a number of routes. Aprotic ILs are distinguished from the protic form both by the method through which they are made, and by the stability of products formed at their cathodic limit. Protic ILs are generally reversibly reduced at their cathodic limit while aprotic ILs are reduced in an irreversible reaction; in our group H^+/H_2 reversibility determines whether and IL is a pIL.

IL Reference Electrodes

A common challenge in non-aqueous electrolytes, and ionic liquids in particular, is the selection of a stable and non-contaminating reference electrode. Frequent choices from the literature include bare silver wires [49], aqueous Ag/AgCl ref-

erence electrodes immersed in the IL [62; 63], and silver triflate solutions [50]. Ag/AgCl is a common aqueous reference potential due to the extremely low solubility of AgCl in aqueous solutions, however it would be false to carry the low AgCl solubility assumption into ionic liquids. Some early experiments in this work attempted to use silver based reference electrodes, but leaking of Ag^+ cations through the porous frit eventually contaminated the IL.

Protic ionic liquids permit the use of the palladium-hydrogen reference electrode which is a distinct advantage. The details of its preparation and thermodynamic potential are discussed in depth by Batista et. al. [7]. The advantage of the Pd/H reference potential comes from it being intrinsically tied to the proton activity within the pIL. The potential defined by 0V vs Pd/H is the potential at which hydrogen is oxidized to protonate the anion, or reduced from the conjugate base: $Pd + HA + e^- \rightarrow Pd/H + A^-$.

In the aprotic IL work presented in Chapters 3 and 4, a psuedo reference potential is used. The potential of a Pt wire in dry oxygen saturated C_4dMImTf was found to be repeatable and stable with respect to the $O_2/O_2^{\bullet -}$ couple. To ensure this potential did not drift with the addition of acids or water, the Pt reference wire was isolated behind a porous glass frit in dry O_2 saturated IL.

Hydrophobic vs Hydrophilic ILs

In literature, ionic liquids are generally classified as either hydrophobic or hydrophilic, though this is misleading because the category of water-stable hydrophilic ILs does not necessarily imply they make good desiccants. In fact, the water content at which ILs are investigated is rarely cited, and this may lead to general uncertainty concerning their melting points and viscosities. A more accurate characterization

is water-miscible or immiscible. The miscibility of an IL with water is predicted based on its structure, assuming that no chemical reactions take place to disturb it. As the total alkyl chain length of the ion increases, its solubility in water decreases. Additionally, increasing the number of fluorines within the structure will also decrease its solubility in water. A representative illustration of this last point is the observation that tetrafluoroborate (BF_4^-) ILs are miscible with water while hexafluorophosphate (PF_6^-) are immiscible.

The Electrode—IL Interface

When an electrode is polarized and no faradaic reaction occurs an excess charge develops on its surface. This condition is referred to as an ideally polarizable electrode. The surface charge density is defined thermodynamically by the change in the Gibbs surface energy with potential as written in the Lippmann equation (Eqn. 2.22). Differentiating the Lippmann equation (Eqn. 2.23) defines the differential capacity of the interface which can be measured using the impedance technique described in Section 2.3. Thus changes in the differential capacitance of the interface directly relate to changes in its state.

$$\sigma^M = -\left(\frac{\delta\gamma}{\delta E}\right)_{T,P,\mu_i} \tag{2.22}$$

$$C = \frac{\delta\sigma^M}{\delta E} = -\left(\frac{\delta^2\gamma}{\delta^2 E}\right)_{T,P,\mu_i} \tag{2.23}$$

term	description	value/unit
σ^M	surface excess charge	C/m^2
γ	Gibbs surface energy	J/m^2
E	electrode potential	volts
C	differential capacity	F/m^2

The surface excess charge on the electrode is completely balanced by a correspond-

ing charge within the solution. The solution structure which develops to support this charge is refereed to as the Electrical Double Layer (EDL) and it is generally less than 10Å thick. A potential drop of 100mV across this distance corresponds to an electric field of order 10^8V/m. Thus the EDL provides a mechanism to produce large electric fields within the electrolyte. It is also closely related to the phenomenon of electrowetting which requires consideration in the design of air cathodes [64; 65].

Double Layer in Dilute Solutions

Over a century ago a capacitive description of the interface that develops between a conducting electrode and an electrolyte was proposed Helmholtz and later elaborated upon by Gouy [66], Chapman [67], Stern [68], and Grahame [69]. Helmholtz initially modeled the interface as a simple capacitor, where a single layer of ions adsorbed on the electrode surface accounted for the excess charge in the polarized electrode (Fig. 2.3a). Gouy's and Chapman's identical but independent contribution accounted for the disorder of the structure due to thermal motion and is analogous to Debye-Huckel theory insofar as the interactions are purely electrostatic, the ions are unpolarizable point charges, and the distribution of ions follows Boltzmann's statistics [70].

Stern combined these theories to create the electrical double layer of dilute electrolytes where a dense compact layer of solvated ions next to the electrode (Stern layer) exists before the electric potential decreases exponentially into the bulk electrolyte. The capacity of the Stern layer is limited by preventing ions from approaching within half an ionic radius of the electrode. Grahame further distinguished between two structures within the Stern layer: a layer of solvent molecules directly

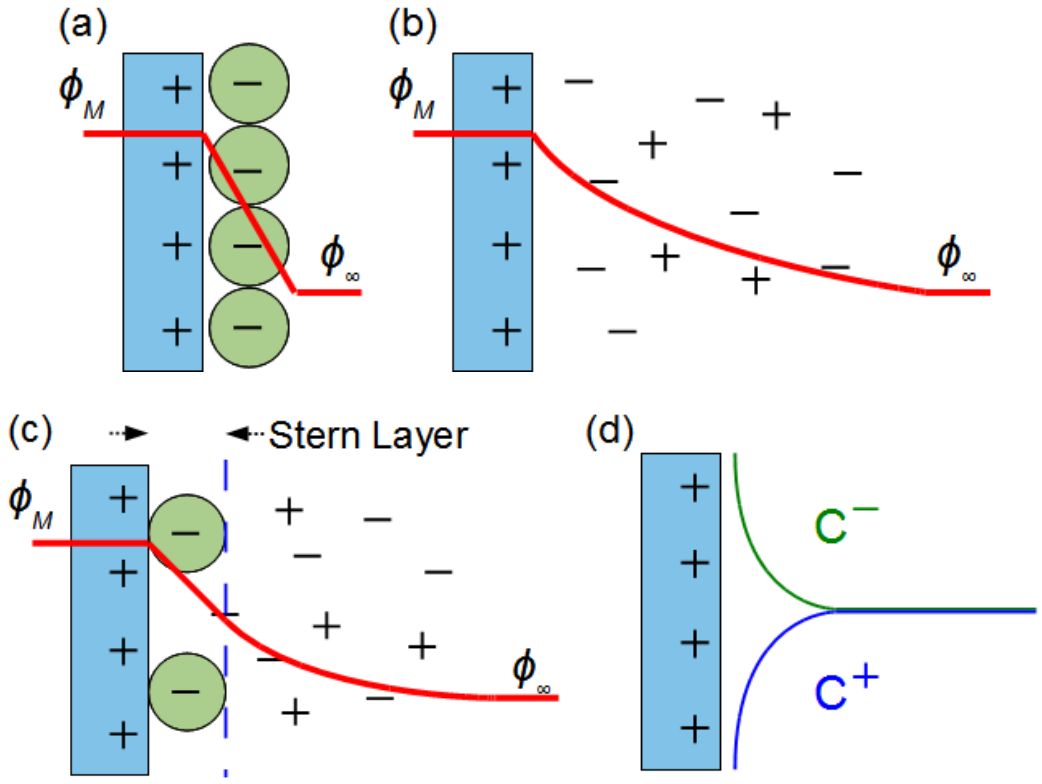

Figure 2.3: Schematic of the electrical double layer in a dilute electrolyte showing the electrochemical potential for the (a) Helmholtz model, (b) Gouy-Chapman model, (c) Stern model, and (d) relative mole fraction of cations and anions when $E > E_{pzc}$.

on the electrode surface termed the inner Helmholtz plane, and a layer of solvated counter ions termed the outer Helmholtz plane. A simple schematic of these models and structures is shown in Fig. 2.3.

To condense the following equations it will be helpful to define a couple common terms used in the Gouy-Chapman based double layer theories. These include a Debye length (Eqn. 2.24) and a dimensionless potential (Eqn. 2.25). It will also be assumed that each ion has a valence, $z = \pm 1$.

$$\frac{1}{L_D} = \sqrt{\frac{4\pi e^2 c_{IL}}{\varepsilon k_B T}} \tag{2.24}$$

$$u = z_e e(\phi_M - \phi_\infty)/k_B T \tag{2.25}$$

term	description	value/unit
L_D	Debye length	cm
e	elementary charge	$1.602 \cdot 10^{-19} C$
c_{IL}	average electrolyte concentration	$mole/cm^3$
ε	dielectric constant of medium	$\varepsilon_0 \varepsilon_r$
k_B	Boltzmann's constant	$8.617 eV/K$
T	temperature	°K
u	dimensionless potential	25mV @ 25°C
ϕ_M	potential at electrode surface	volts
ϕ_∞	potential in bulks solution	volts

The potential decay through the diffuse layer more or less follows the form of equation 2.26 assuming equal valence ions, though it is more accurately given by Eqn. 2.27 following a derivation through Boltzmann's statistics [70].

$$\phi(x) = [\phi_M - \phi_\infty] \cdot e^{-x/L_D} \tag{2.26}$$

$$\frac{\delta\phi}{\delta x} = -\frac{k_B T}{L_D} \cdot \sinh\left(\frac{u}{2}\right) \tag{2.27}$$

term	description	value/unit
ϕ	potential	Volts
L_D	Debye length	cm
ε	dielectric constant of medium	$4\pi\varepsilon_0\varepsilon_r$
k_B	Boltzmann's constant	$8.617 eV/K$
T	temperature	°K
u	dimensionless potential	volts

Poisson's equation (Eqn. 2.28) is then used to determine the total charge within the diffuse layer (Eqn. 2.29).

The Gouy-Chapman capacity is finally derived using the Lipmann equation and differentiating Eqn. 2.29 to arrive at Eqn. 2.30.

$$\frac{\delta^2\phi(x)}{\delta x^2} = -\frac{4\pi\rho(x)}{\varepsilon} \tag{2.28}$$

$$\begin{aligned}\sigma^M &= -\frac{\varepsilon}{4\pi}\int_M^\infty \rho(x)dx \\ &= -\frac{\varepsilon}{4\pi}\left(\frac{\delta\phi}{\delta x}\right)_{x=M} \\ &= \frac{\varepsilon k_B T}{4\pi L_D}\cdot\sinh\left(\frac{u}{2}\right)\end{aligned} \tag{2.29}$$

term	description	value/unit
ϕ	potential	Volts
ρ	volumetric charge density	C/cm^3
σ^M	surface excess charge	C/cm^2
L_D	Debye length	cm
ε	dielectric constant of medium	$\varepsilon_0\varepsilon_r$
k_B	Boltzmann's constant	$8.617eV/K$
T	temperature	°K
u	dimensionless potential	volts

$$\begin{aligned}C_{GC} &= \frac{\delta\sigma^M}{\delta\phi} \\ &= \frac{\varepsilon}{4\pi L_D}\cdot\cosh\left(\frac{u}{2}\right)\end{aligned} \tag{2.30}$$

term	description	value/unit
C_{GC}	Gouy-Chapman capacitance	F/cm^2
ϕ	potential	Volts
σ^M	surface excess charge	C/cm^2
L_D	Debye length	cm
ε	dielectric constant of medium	$\varepsilon_0\varepsilon_r$
u	dimensionless potential	volts

Combining the Gouy-Chapman capacity with the Helmholtz capacity in series provides a good approximation for the real differential capacitance of dilute aqueous electrolytes [69]. The Helmholtz capacity is usually estimated from experiments performed in concentrated electrolytes and dominates when $(\phi_M - \phi_\infty)$ is large.

$$\frac{1}{C_{obs}} \approx \frac{1}{C_H} + \frac{1}{C_{GC}} \tag{2.31}$$

term	description	value/unit
C_{obs}	observed capacity	F/m^2
C_H	Helmholtz capacity	F/m^2
C_{GC}	Gouy-Chapman capacity	F/m^2

Owing to the fact that these EDL models are based upon the Boltzmann equation, the differential capacity is correctly predicted to decrease with increasing temperature as the EDL becomes more diffuse from increased thermal disruption. Conversely, the differential capacity of ILs has been observed to increase with temperature [71]. A summary of the current understanding of the EDL in ILs is developed in Section 2.2.

Double Layer of ILs

Ionic liquids are not dilute electrolytes, they all have large molar volumes, the molar volume of the anion and cation are rarely equal, the diffuse charges on asymmetric ions make them polarizable, and there is no separate solvent to screen charges. This greatly complicates the interfacial structure and differential capacitance. While a solid understanding the interface between planar metal electrodes and ILs is still being developed [71–79], a reasonable explanation of their unique capacitive response is available.

Early accounts of the ionic liquid double layer [80] were given in the framework of high temperature molten salts [81–83]. These studies suggested that the capacitance is at a minimum at the PZC, a quality shared with dilute aqueous electrolytes. However it became clear that the diffuse model developed by Stern, Gouy, and Chapman is not applicable to these concentrated systems due to both the high ca-

pacities measured ($> 20\mu F/cm^2$) and the increase in capacitance with temperature. In high temperature molten salts, an attempt to salvage the Gouy-Chapman behavior was attempted by theorizing that the capacitive behavior was set by cationic or anionic vacancies which followed Boltzmann's statistics. This vacancy theory was only successful at predicting the capacitive response of molten salts where the anions and cations were of approximately equal size [84].

Stillinger et. al. produced an early description of the double layer region in concentrated electrolytes by accounting for both the ion size and the electrostatic interaction between ions [85]. Accounting for these phenomena results in a double layer much thicker than predicted for dilute electrolytes. This is due not only to lower density through ionic volume, but also an ordering that results from the electrostatic interaction: the interface is composed of a lattice-like structure of alternating anion and cation layers. If these cations and anions are of equivalent size then the resulting differential capacity is expected to be symmetric about the PZC. The increase in capacity with greater polarization away from the PZC is associated with compression of these alternating layers whereas at the PZC there is no net charge within the structure.

Gale and Osteryoung theorized in 1980 that ILs also have exceptionally high capacities due to the higher surface coverages when solvent molecules are absent [80]. This would result in a complete absence of the inner Helmholtz plane found by Grahame in dilute aqueous solutions and potentially enable higher catalytic efficiencies due to larger exchange currents. When examining chloroaluminate melts it was found that basic melts ($[AlCl_4^-] > [Al_2Cl_7^-]$) had higher capacities near the PZC than their acidic counterparts. This was attributed to larger surface coverage attainable with the smaller $AlCl_4^-$ anion.

The differential capacitance of current generation ILs (those that are air and water stable) remained largely uninvestigated until the work of Nanjundiah in 1997 [84] who observed that no contemporary theory could explain the increase in capacity with temperature. Nanjundiah also regretfully observed that the electrocapillarity maximum, frequently used to define the PZC, did not necessarily correspond to the capacitive minimum.

After close to three decades of neglect, the theory of the double layer in ILs leapt forward with new model developed by Kornyshev [72] which more closely resembles Fermi-Dirac statistics rather the Boltzmann background of Gouy-Chapman. This basic change places an upper bound on the local concentration of ions and begins to account for ion volume. Beginning with the ionic distribution given in Eqn. 2.32:

$$c_{\pm} = \frac{c_{IL}}{2} \cdot \frac{e^{-u}}{1 - \frac{c_{IL}}{c_{max}} + \frac{c_{IL}}{c_{max}} \cosh(u)}, \tag{2.32}$$

term	description	value/unit
$c_{\pm}$	concentration of cations or anions	$moles/L$
c_{IL}	average concentration of IL	$moles/L$
c_{max}	maximum local concentration	$moles/L$
u	dimensionless potential	volts

which is used to determine the charge density in Eqn 2.33. The $\frac{c_{IL}}{c_{max}}$ describes the compressibility of the IL under an electric field, where c_{IL} is the bulk molar density and c_{max} is the maximum attainable (estimated to be $2 \cdot c_{IL}$ for ions of equal molar volume).

Finally the Poisson equation is used to relate the charge density to the potential distribution through the double layer in Eqn. 2.34.

$$\rho = e(c_+ - c_-) = -4ec_{IL}\frac{\sinh(u)}{1+2\frac{c_{IL}}{c_{max}}\sinh^2\left(\frac{u}{2}\right)}, \tag{2.33}$$

term	description	value/unit
ρ	charge density	C/L
c_+	cation concentration in EDL	$moles/L$
c_-	anion concentration in EDL	$moles/L$
c_{IL}	average concentration of IL	$moles/L$
c_{max}	maximum local concentration	$moles/L$
e	elementary charge	$1.602 \cdot 10^{-19} C$
u	dimensionless potential	volts

$$\begin{aligned}\frac{\delta^2\phi}{\delta x^2} &= -\frac{4\pi\rho}{\varepsilon} \\ &= \frac{16ec_{IL}}{\varepsilon}\frac{\sinh(u)}{1+\frac{2c_{IL}}{c_{max}}\sinh^2\left(\frac{u}{2}\right)},\end{aligned} \tag{2.34}$$

term	description	value/unit
ϕ	potential relative to ϕ_∞	Volts
ρ	charge density	C/L
c_{IL}	average concentration of IL	$moles/L$
c_{max}	maximum local concentration	$moles/L$
e	elementary charge	$1.602 \cdot 10^{-19} C$
ε	dielectric constant of medium	$4\pi\varepsilon_0\varepsilon_r$
u	dimensionless potential	volts

Kornyshev concludes his derivation by solving for a new expression for the double layer capacitance as Eqn. 2.35, which reduces to the Gouy-Chapman result in Eqn. 2.30 for dilute electrolytes when $c_{max} \gg c_{IL}$.

This final expression for the differential capacity of an electrode immersed in an ionic liquid results in the PZC coinciding with the maximum capacity. The maximum concentration condition also predicts a different interfacial structure for the IL. The two local maxima predicted by Kornyshev's model move closer together as the concentration of the IL is increased until a point where they merge [71]. This

$$C = \frac{\varepsilon}{4\pi L_D} \cdot \frac{\cosh\left(\frac{u}{2}\right)}{1 + 2\frac{2c_{IL}}{c_{max}}\sinh^2\left(\frac{u}{2}\right)} \cdot \sqrt{\frac{2\frac{2c_{IL}}{c_{max}}\sinh^2\left(\frac{u}{2}\right)}{\ln\left[1 + 2\frac{2c_{IL}}{c_{max}}\sinh^2\left(\frac{u}{2}\right)\right]}} \tag{2.35}$$

term	description	value/unit
L_D	Debye length	cm
c_{IL}	average concentration of IL	$moles/L$
c_{max}	maximum local concentration	$moles/L$
ε	dielectric constant of medium	$4\pi\varepsilon_0\varepsilon_r$
u	dimensionless potential	volts

has important potential implications for the work presented in Chapter 4 in which water is added to the IL potentially diluting it.

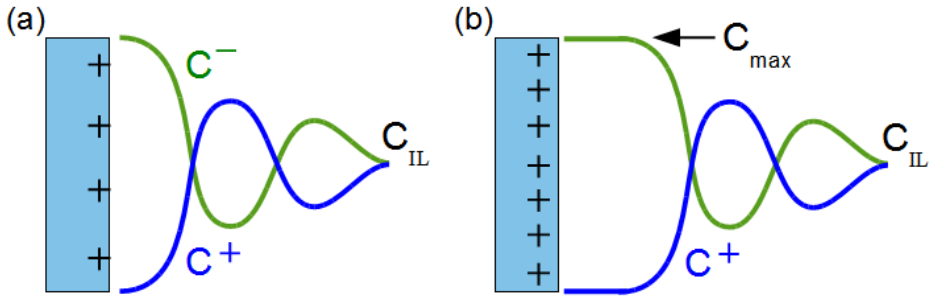

Figure 2.4: Schematic of the electrical double layer in an ionic liquid showing the concentration profiles for cations and anions on a (a) moderately polarized electrode (200mV) and (b) heavily polarized electrode (2.0V).

Figure 2.4 represents the concentration profile for two electrodes polarized at different charge densities showing the overscreening (Fig. 2.4a) and crowding phenomena (Fig. 2.4b). Overscreening occurs at moderate polarizations and is associated with a local maximum in the differential capacitance curve, while crowding results in a diminished capacitance at high polarizations [78]. In both cases concentration oscillations exist in the EDL. These have been observed to extend as far as seven ionic layers into the bulk electrolyte at a polarization of 2.0V [79]. It is the thin-

ning of this structure with increasing temperature which results in the increase in capacitance [86].

An excellent and critical interpretation of Kornyshev's model was tested experimentally on a wide range of ionic liquids by Vera Lockett et. al. [71]. A criticism specific to Kornyshev is that the dielectric constant is invariant with structure and ionic density. Lauw et. al. developed a separate model in which the ions are polarizable and the local dielectric constant is permitted to change with composition [75]. Unlike Kornyshev's work, the differential capacitance predicted by Lauw's model contains two local maxima regardless of the ion concentration.

Lockett also cautions that no model has yet accounted for specific adsorption, and that aqueous results regarding adsorbing ions are not a good proxy because there is no desorption of solvent to overcome. Finally, the large asymmetric ions common to ILs may significantly change their configuration on the electrode surface as the potentials change, e.g. imidazolium could lay perpendicular or flat along the electrode surface depending on potential.

2.3 Electrochemical Techniques

A number of electrochemical methods are well adapted to the investigation of the oxygen reduction mechanism. Generally these control the thermodynamic driving force (potential) and measure the resulting reaction rate (current). Two of the most common are chronoamperometry (CA) and cyclic voltammetry (CV).

Chronoamperometry

In its simplest form, chronoamperometry is the recording of the current response to an abrupt and large change in the electrochemical potential. With a strong enough

driving force, the electron transfer effectively occurs instantaneously and the surface concentration of reactants is zero. In this case, the reaction rate and current response is limited by the flux of oxygen to the electrode surface. This current is described in time by the Cottrell equation shown in Eqn. 2.36.

$$\begin{aligned} i(t) &= \frac{nFA\sqrt{D}C_o}{\sqrt{\pi t}} \\ &= \frac{nFA\sqrt{D}\cdot[mM]\times 10^{-6}}{\sqrt{\pi t}} \end{aligned} \tag{2.36}$$

term	description	value/unit
$i(t)$	current transient	amps
n	number of electrons transferred	#
F	Faraday's constant	96485.3 C/mol
A	surface area	cm^2
C_o	bulk concentration	$mole/cm^3$
D	diffusivity	cm^2/s
t	time	seconds

Cyclic Voltammetry

Cyclic voltammetry controls a repeating linear ramp in the electrochemical potential and monitors the current required to maintain the potential at any point. The recorded data is plotted as current with respect to potential. Different reactions can be observed and their qualitative kinetics evaluated by controlling the potential sweep rate and limits. Fig. 2.5 shows an example of a cyclic voltammagram, plotted both versus time and the typical current versus potential. In the convention used in this document, reduction corresponds to a negative current and negative potentials are more strongly reducing.

Linear sweep voltammetry (LSV) differs from cyclic voltammetry in that only a single scan of the potential window is performed. This prevents the products of

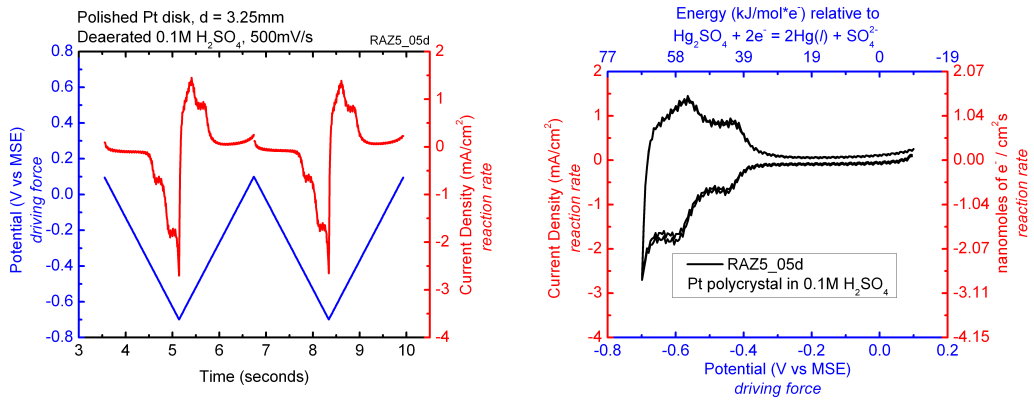

Figure 2.5: Cyclic voltammagram of hydrogen UPD on a platinum disk in 0.1M H_2SO_4 at a scan rate of 500mV/s.

a previous sweep from potentially influencing the features of subsequent scans. Fig. 2.6 is a LSV of oxygen reduction on a polished polycrystalline disk in 0.1M H_2SO_4. The reduction of oxygen begins at a potential slightly above 0.2V vs the mercury/mercurous sulfate reference electrode (MSE) and accelerates with decreasing potential until the dissolved oxygen near the electrode is exhausted. At this point the current is limited by the rate at which oxygen can diffuse to the electrode surface. Some hydrogen adsorption current becomes visible at potentials below -0.4V.

Electron Transfer Kinetics and the Butler-Volmer Equation

Under some conditions, particularly when over potentials are low, concentrations are high, or diffusion distances very small, the rate of an electrochemical reaction is limited by the electron transfer kinetics and not transport of reactants to the electrode surface. At equilibrium, no net reaction occurs: the rate of the forward and reverse reactions are equal. Upon polarization of the electrode the activation energy for electron transfer is biased in proportion with number of electrons trans-

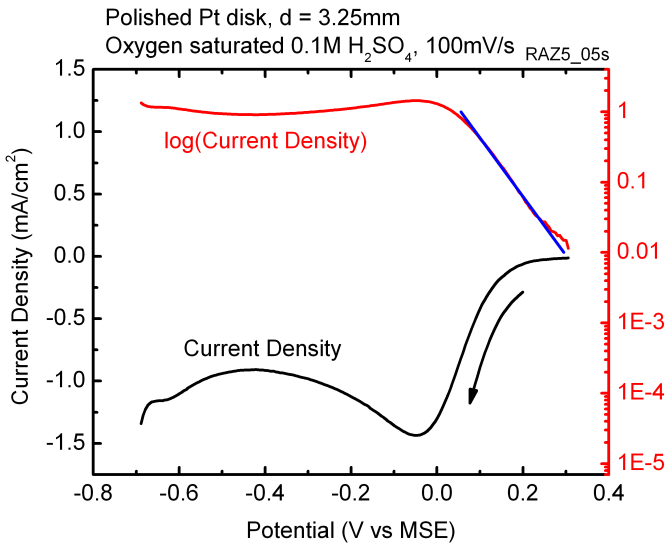

Figure 2.6: Linear sweep voltammagram of Oxygen reduction on polycrystalline Pt in 0.1M H_2SO_4 at 100mV/s and corresponding Tafel slope of 120mV/decade.

fered. This is shown schematically for an oxidation reaction in Fig. 2.7, where ΔG_a is the activation barrier at equilibrium, z^- is the oxidation state of the reduced species, F is Faraday's constant, ΔE is the polarization away from the equilibrium potential, $n = z^+ - z^-$ is the number of electrons transfered, and ΔG_O and ΔG_R are the activation barriers for the oxidation and reduction reactions, respectively.

The activation energy for the oxidation reaction shown schematically in Fig. 2.7 only decreases by a fraction of the energy difference $nF\Delta E$. This fraction is called the charge transfer coefficient and represents the fraction of the Gibbs energy operating on the transition state: $\alpha = (\Delta G_a - \Delta G_O)/nF\Delta E$. Including this concept permits the activation energies to be written as Eqn. 2.37 and Eqn. 2.38 for oxidation and reduction, respectively.

The activation energies are then incorporated with the Arrhenius equation to determine the forward and reverse reaction rates in Eqn. 2.39 and Eqn. 2.40.

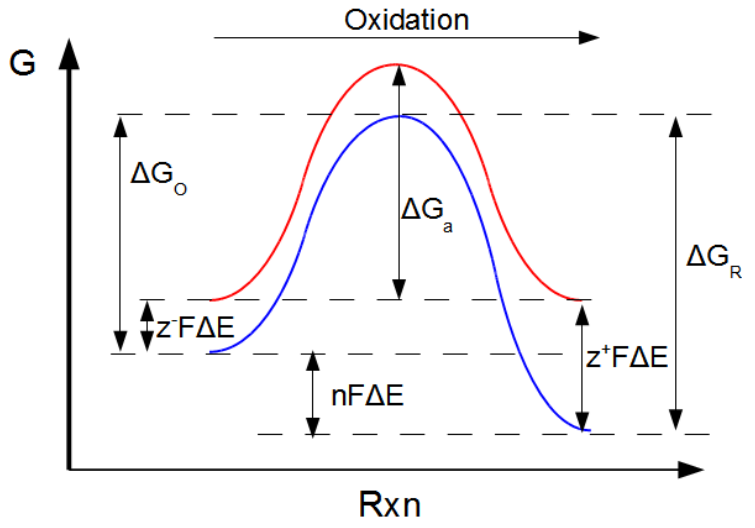

Figure 2.7: Schematic showing how the activation energy for an oxidation reaction changes due to electrode polarization.

$$\Delta G_O = \Delta G_a - \alpha n F \Delta E \tag{2.37}$$

$$\Delta G_R = \Delta G_a - (1-\alpha) n F \Delta E \tag{2.38}$$

term	description	value/unit
ΔG_O	activation energy for oxidation	J/mol
ΔG_R	activation energy for reduction	J/mol
ΔG_a	activation energy at equilibrium	J/mol
α	charge transfer coefficient	$0 \leq \alpha \leq 1$
n	number of electrons	#
F	Faraday's constant	96485.3 C/mol
ΔE	over potential from equilibrium	Volts

The net current is simply the sum of the forward and reverse reaction rates.

If the current is sufficiently small such that the mass transfer rate is effectively infinite, and if the volume of solution is large enough that the reactions do not effect the bulk concentration, then Eqn. 2.43 becomes the Butler-Volmer equation (Eqn. 2.44). This clearly shows that current density increases exponentially with overpotential, and that the steepness of this rise depends on the number of electrons

$$k_O = Ke^{\alpha nF\Delta E/RT} \tag{2.39}$$

$$k_R = Ke^{-(1-\alpha)nF\Delta E/RT} \tag{2.40}$$

term	description	value/unit
k	reaction rate	s^{-1}
K	exponential pre-factor	s^{-1}
α	charge transfer coefficient	$0 \leq \alpha \leq 1$
n	number of electrons	#
F	Faraday's constant	96485.3 C/mol
ΔE	over potential from equilibrium	Volts
R	universal gas constant	8.314 $JK^{-1}mol^{-1}$
T	temperature	°K

$$i_{net} = i_O - i_R \tag{2.41}$$

$$= nFAk_O C_O - nFAk_R C_R \tag{2.42}$$

$$= nFAK\left[C_O e^{\alpha nF\Delta E/RT} - C_R e^{-(1-\alpha)nF\Delta E/RT}\right] \tag{2.43}$$

term	description	value/unit
i	current	amps
A	surface area	cm^2
C	concentration	$moles/L$
k	reaction rate	s^{-1}
K	exponential pre-factor	s^{-1}
α	charge transfer coefficient	$0 \leq \alpha \leq 1$
n	number of electrons	#
F	Faraday's constant	96485.3 C/mol
ΔE	over potential from equilibrium	Volts
R	universal gas constant	$8.314JK^{-1}mol^{-1}$
T	temperature	°K

transferred, n, and the charge transfer coefficient, α. For a reversible reaction with $\alpha = 0.5$, the anodic and cathodic branches of the net current are symmetrical. In contrast, the exchange current density, j_0, affects both reactions equally and merely determines their magnitude.

$$j(\Delta E) = j_0 \left[e^{\frac{\alpha nF}{RT} \cdot \Delta E} - e^{-\frac{(1-\alpha)nF}{RT} \cdot \Delta E} \right] \tag{2.44}$$

$$\log |j| = \log j_0 + \frac{\alpha nF}{2.303RT} \cdot |\Delta E| \tag{2.45}$$

term	description	value/unit
$j(\Delta E)$	current density	$amps/cm^2$
ΔE	overpotential	Volts
j_0	exchange current density	$amps/cm^2$
α	charge transfer coefficient	$0 \leq \alpha \leq 1$
n	number of electrons transferred	#
F	Faraday's constant	96485.3 C/mol
R	gas constant	8.3144 $Jmol^{-1}K^{-1}$
T	absolute temperature	$^\circ K$

Equation 2.45 is a modified form of the Tafel equation written for the oxidation reaction, and is valid for $|\Delta E| \gg \frac{RT}{nF}$ ($\gtrsim 25/n$ mV at 25°C) provided the current is entirely determined by the electron transfer rate. By plotting the logarithmic current versus overpotential, such as the red curve and axis of Fig. 2.6, it is possible to extract the Tafel slope and exchange current density. The Tafel slope, which is derived from the exponential of the Bulter-Volmer equation, is indicative of the rate limiting step of the reaction. The blue line drawn in Fig. 2.6 has a slope of 120mV/decade which corresponds to the rate limiting step being a single electron transfer, and intercepts the open circuit potential at a current density of approximately $7 \times 10^{-3} mA/cm^2$. This intercept is in close agreement with the literature value for exchange current density of ORR on Pt in H_2SO_4 [87], confirming the cleanliness of the Pt surface. Exchange current density is frequently used in the evaluation of catalyst activity, where a larger j_0 implies a more effective catalyst.

Rotating Ring-Disk Electrodes

Rotating ring-disk electrodes (RRDE) permit control of reactant transport. This is accomplished by spinning the electrode at a rapid rate which creates a radial flux and corresponding laminar convective flow. The flow draws fresh electrolyte from the bulk to the electrode surface and sweeps the reaction products past the ring. By controlling the ring potential independently of the disk it is possible to identify the reaction products.

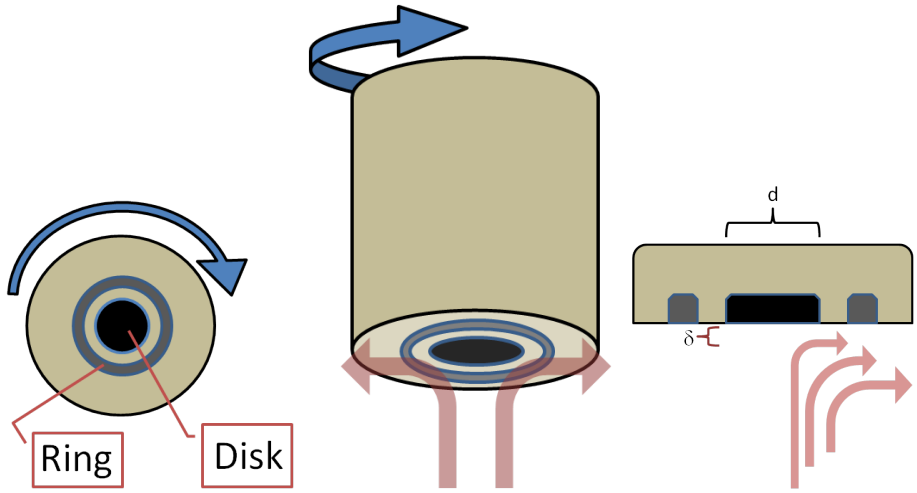

Figure 2.8: Schematic of the rotating ring-disk electrode geometries. δ refers to the diffusion layer thickness which decreases with increasing rotation rate.

RRDE was notably used by Ross [20] to determine the origin of hydrogen peroxide production on platinum during ORR in aqueous acid. Reproduced in Fig. 2.9 is Ross' figure for Pt(111). In this experiment, cyclic voltammetry was performed on the disk electrode while the ring was held at a constant potential at which H_2O_2 would be oxidized.

As the potential is swept negative in the main plot, the oxygen reduction current increases due to the stronger driving force. Eventually the reaction rate becomes

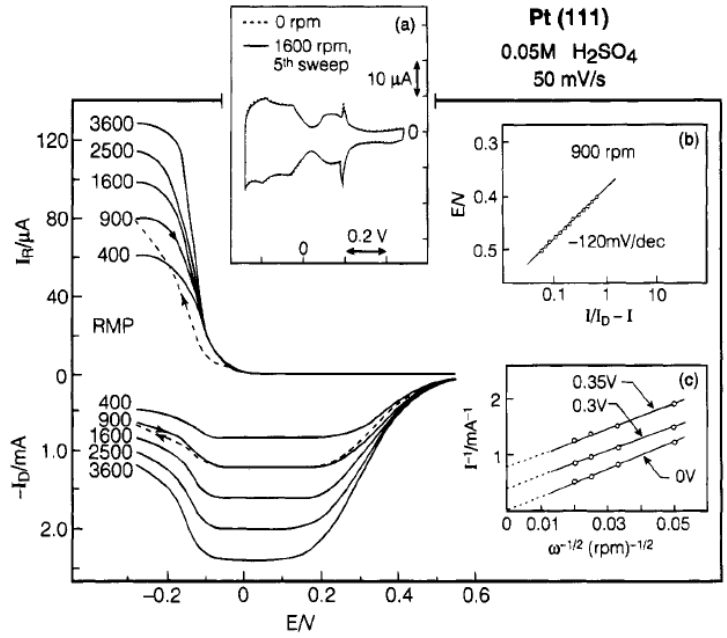

Figure 2.9: RRDE of oxygen reduction in 0.05M H_2SO_4 on a Pt(111) single crystal at 50mV/s vs an SCE reference. Inset (a) shows hydrogen UPD on the Pt surface in a deaerated solution, (b) is the Tafel plot, and (c) the Koutecky-Levich plot of the limiting current. Reprinted with permission from *J. Phys. Chem.*, 1995, 99 (11), pp 3411-3415. Copyright 1995 American Chemical Society.

limited by the transport of oxygen to the electrode surface and the current remains constant with potential. However, the magnitude of the reduction current decreases once the potential is swept below 0.1V. This potential corresponds with the adsorption of hydrogen on the Pt(111) surface, shown in inset (a) which inhibits the complete reduction of O_2. The solvated H_2O_2 is then swept away by the convective flow and is oxidized at the ring electrode. The ring electrode shows an increase in oxidation current concurrent with the decrease in disk reduction current.

The mass transport limited current, i_L, is controlled by the flux of oxygen through the diffusion boundary layer shown in Eqn. 2.46. The thickness of the diffusion boundary layer, δ, is well defined and uniform during laminar flow and is a function

$$i_L = \frac{nFAD}{\delta} C_o \tag{2.46}$$

$$= 0.62nFAD^{2/3}\omega^{1/2}\nu^{-1/6}C_o \tag{2.47}$$

$$= 0.62nFAD^{2/3}\left[\frac{2\pi}{60}\cdot rpm\right]^{1/2}\nu^{-1/6}\cdot[mM]\times 10^{-6}$$

$$\frac{1}{i_{tot}} = \frac{1}{i_k} + \frac{1}{i_L} \tag{2.48}$$

$$= \frac{1}{i_k} + \frac{1}{0.62nFAD^{2/3}\omega^{1/2}\nu^{-1/6}C_o} \tag{2.49}$$

term	description	value/unit
i_L	limiting current	amps
i_{tot}	total current	amps
i_k	kinetic current	amps
n	total electrons transferred	#
F	Faraday's constant	96485.3 C/mol
A	surface area	cm^2
D	diffusivity	cm^2/s
δ	diffusion layer thickness	cm
C_o	bulk concentration	$mole/cm^3$
ω	angular velocity	s^{-1}
ν	kinematic viscosity	cm^2/s

of angular velocity. Equation 2.46, when modified to state the diffusion boundary thickness as a function of solution properties and rotation rate, becomes Equation 2.47: the Levich equation. The rate at which the limiting current changes with rotation rate can be used to extract specific details about the number of electrons transferred in the overall reaction, the concentration of electroactive species, or the diffusion constant of the reactants. Further analysis of the time delay between events on the disk and events on the ring can provide a rough estimation of the diffusivity of the products [88].

More generally, the Koutecky equation (Eqn. 2.48) defines the total current as the inverse sum of the kinetic current and mass transport limited current. By simply combining it with the Levich equation, a relationship is derived (Eqn. 2.49) which

allows the determination of the electron-transfer limited current as a function of potential by extrapolating to an infinite mass transport rate. This analysis is plotted in inset (c) of Fig. 2.9, where the intercept at $\omega^{-1/2} = 0$ is the pure kinetic current at a given potential.

Microelectrodes

While RRDE permits the explicit control of reactant transport to the electrode, this is also accomplished by varying the geometry of the electrode. The one-dimensional diffusion of electroactive species to a large smooth planar electrode in a static solution was described previously by Eqn. 2.36 in which the current transient was proportional to $\sqrt{Dt^{-1}}$. However, by using a spherical electrode, such as a hanging drop of mercury, a constant term is added to the Cottrell equation in which current scales linearly with D and inversely with the sphere radius. At long times, providing convection is avoided, the current approaches a steady state value equal to this constant.

Disk microelectrodes behave similarly. A microelectrode generally has a characteristic radius less than 25μm which permits hemispherical diffusion to the electrode surface. Exploiting this geometry, Shoup and Szabo have developed an empirical expression (Eqn. 2.50) which describes the current as the function of a dimensionless time parameter, τ, with fair accuracy [89]. At short times the current decays rapidly while at long times it approaches a steady state value due to hemispherical diffusion. By exercising the different scaling with diffusivity, microelectrode chronoamperometry compared with the planar Cottrell equation will deconvolute nC and D in a given system. Deviations from ideal Cotrellian behavior have been used to elucidate the chemical rate constants for ECE mechanisms [90].

$$i(\tau) = -4nFDC_o r_d f(\tau) \tag{2.50}$$
$$f(\tau) = 0.7854 + 0.8863\tau^{-1/2} + 0.2146e^{-0.7823/\sqrt{\tau}}$$
$$\tau = \frac{4Dt}{r_d^2}$$

term	description	value/unit
$i(\tau)$	current transient	amps
n	number of electrons transferred	#
F	Faraday's constant	96485.3 C/mol
A	surface area	cm^2
C_o	bulk concentration	$mole/cm^3$
D	diffusivity	cm^2/s
r_d	micro-disk radius	cm
t	time	seconds

Cyclic voltammetry is also effected by the diffusion geometry of a microelectrode: the diffusion limited current is larger and the curve does not contain a depletion induced peak. Another result of the rapid diffusion is a general lack of reversible peaks, regardless of whether the electrochemical reactions themselves are reversible. On a large electrode with planar diffusion, the products of an electrochemical reaction are still accessible during the return sweep of a cyclic voltammagram. In contrast, the diffusion distance from and *to* the bulk electrolyte is much shorter on a micro electrode and reaction products generally diffuse into the bulk of the solution. Therefore, reversible reactions during a cyclic voltammagram on a microelectrode imply the production of insoluble or adsorbed species.

Differential Capacitance through Impedance

The impedance of an electrochemical cell is the complex form of its resistance. It is measured by determining the drop in voltage across an impedance Z for a given current, as well as the time lag between the current and voltage signals. This is fre-

quently accomplished with a sinusoidal potential wave form of the type represented by Eqn. 2.51 and recorded as the response through Eqn. 2.52. The impedance is defined as the ratio of these two quantities (Eqn. 2.53) and is expressed as a magnitude, Z_o, and phase shift, ϕ. The magnitude of the impedance and the phase shift are visualized simultaneously in a Lissajous curve as shown in Fig. 2.10.

$$E = E_0 \sin(\omega t) = E_0 e^{\iota \omega t} \tag{2.51}$$

$$I = I_0 \sin(\omega t + \phi) = I_0 e^{\iota \omega t + \phi} \tag{2.52}$$

$$Z(\omega) = \frac{E}{I} = Z_0 e^{\iota \phi} = Z_0(\cos\phi + \iota \sin\phi) \tag{2.53}$$

term	description	value/unit
E	instantaneous potential	volts
E_0	amplitude of perturbation	volts
ω	frequency	$2\pi f$
ϕ	phase lag of current	s^{-1}
Z	impedance	ohms
ι	imaginary unit	$\sqrt{-1}$

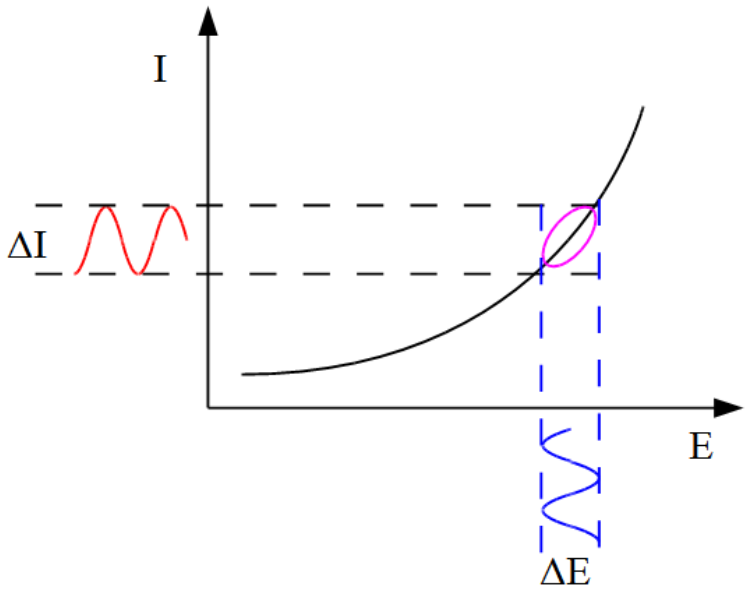

Figure 2.10: Origin of the Lissajous curve in electrochemical impedance showing how the potential perturbation affects the current response.

Differential capacitance is an important technique for characterizing the electrochemical double layer, including the presence of adsorbates and the potential of zero charge (PZC). It is a measure of the surface charge density variation with potential and electrochemical impedance methods are available to measure the capacitance as a function of potential. The total electrochemical impedance consists of the ohmic resistance of the electrolyte, R, in series with the double layer capacitance, C, as shown in Equation 2.54.

$$Z = Z_{Re} + \imath Z_{Im} = R + (\imath C\omega)^{-1} \qquad (2.54)$$
$$C = -(\omega Z_{Im})^{-1}$$

term	description	value/unit
Z	total impedance between WE and RE	ohms
Z_{Re}	real component of impedance	ohms
Z_{Im}	imaginary component of impedance	ohms
$\imath$	imaginary unit	$\sqrt{-1}$
R	electrolyte resistance	ohms
C	capacitance	F/m^2
ω	frequency of AC perturbation	s^{-1}

Unfortunately, the capacitance of polycrystalline and amorphous solid electrodes is not independent of the AC perturbation frequency [91]. Differential capacitance measurements made in ILs typically use frequencies between 0.1kHz and 2.0kHz and result in capacitances between $5\mu F/cm^2$ and $60\mu F/cm^2$ depending on temperature and molar volume of the ionic liquid [73; 75]. Higher homologous temperatures and smaller ions result in larger measured capacitances [71; 74; 76].

The differential capacitance curve of an ionic liquid looks much more complicated than its aqueous counterpart. This double peaked curve has been termed "camel shaped" after the Bactrian camel of the Gobi desert (not the Dromedary camel of Arabia) [77]. *Nem hasznos!*, as a Hungarian would say. A plot of the differen-

tial capacitance on GC in C_4dMImTf illustrates this shape in Fig. 2.11. This data contains a capacity minimum for GC in C_4dMImTf at ca. -800mV vs the Pt std. reference with cation adsorption giving rise the local maximum at -1.05V and anion adsorption dominating at -0.55V.

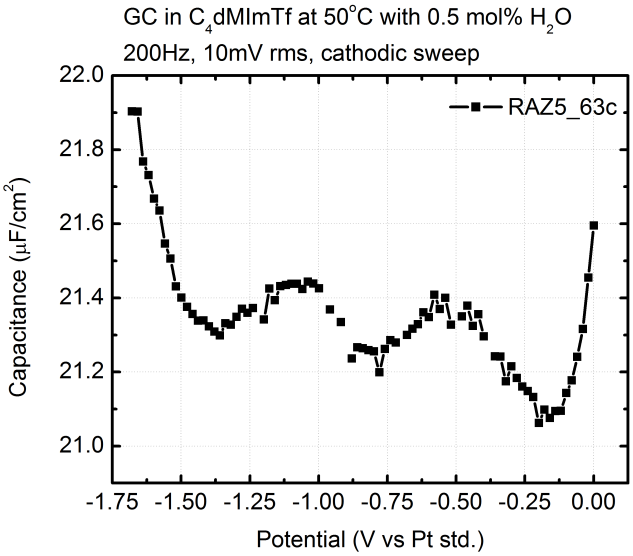

Figure 2.11: Differential Capacitance of a polished GC electrode in C_4dMImTf at 50°C. Taken from the imaginary impedance collected every 20mV using a 10mV AC potential oscillation at 200Hz. Outlier data points omitted.

Table 2.2 summarizes the majority of the electrochemical techniques used in the performance of this work and the information they can provide.

2.4 ORR in the Protic Ionic Liquid TEATf

Among ionic liquids, the protic variety allow for analogies with reactions observed in aqueous systems, and their water miscibility can easily be designed by carefully selecting the anion. The relatively high vapor pressure of their components, coupled with the minuscule vapor pressure of the associated ion pair, makes pIL purification relatively simple. Typically the cation of a pIL is a stronger proton donor than

Technique	Analysis	Reveals
Cyclic voltammetry	varying scan rate	presence of adsorbates
	Tafel	n in rate limiting step
Chronoamperometry	Cottrell	$nC\sqrt{D}$
	Shoup and Szabo	nCD
RDE	Levich	$nCD^{2/3}$
	Koutecky-Levich	$nCD^{2/3}$ and i_k
Mott-Shottkey Impedance	Differential Capacitance	double layer structure

Table 2.2: Summary of electrochemical techniques and a selection of information obtained from them.

water. Thus oxygen reduction in pILs and ORR in weakly acidic ($pH > 4$) aqueous systems are similarly understood.

Many properties of pILs, including the effective pH which influences the oxygen reduction mechanism, are determined by the difference in pK_a between the donor acid and accepting base . The consequences of differences in pK_as have been investigated in detail by Angell [59; 60; 92], Bautista [7], and Watanabe [93]. Watanabe has further pursued the behavior of oxygen reduction in pILs with particular attention to their suitability to hydrogen fuel cells [94].

Lei Tang et al. have also investigated the mechanism of oxygen reduction in pILs [61]. This work made extensive use of the rotating disk electrode to develop a full reaction scheme and postulate some likely ORR intermediates. It is her work concerning ORR in TEATf that is analysed here in Section 2.4.

TEATf was prepared according to the procedure reported by Belieries [95] which involves the addition of triflic acid (HTf) to a slight molar excess of the base triethylamine (TEA) followed by a period under vacuum in which the volatile excess base is removed. This ensures a stoichiometric liquid with no excess acid and keeps the IL dry (< 300 ppm H_2O).

Catalysts for ORR in TEATf

Earlier in this document (Fig. 2.2) the intrinsic background reactions on Pt in deaerated TEATf were shown and explained. Fig. 2.12 contains cyclic voltammagrams of oxygen reduction in TEATf on polycrystalline Pt, Ag, Au and Pd at 100mV/s and 75°C. All subplots within this figure are plotted on the same scale for comparison.

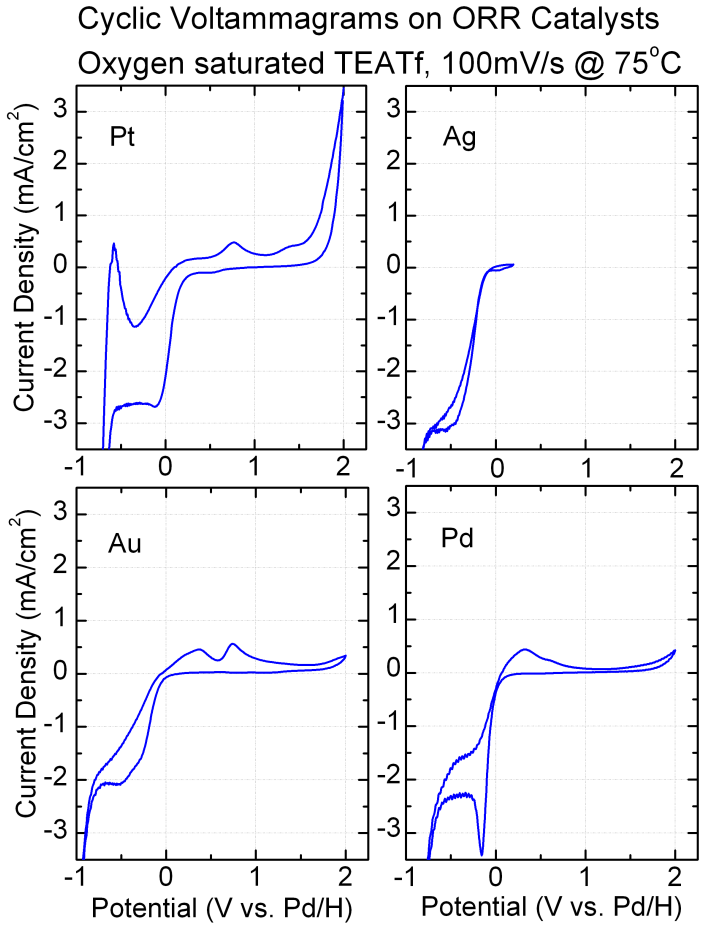

Figure 2.12: Cyclic voltammagrams on Pt, Ag, Au, and Pd in oxygen saturated TEATf at 100mV/s and 75°C. Data replotted from reference [61].

Oxygen reduction on Pt begins at approximately +0.38V vs Pd/H and becomes diffusion limited by -0.1V. Hydrogen evolution due to the deprotonation of the amine

base begins to dominate below -0.55V. Upon cycling positive, the familiar oxidative peak due to hydrogen gas oxidation is clearly visible, followed by the arrest of oxygen reduction and a small oxidation wave at +0.75V. The anodic limit of the IL is visible just positive of the potential at which the Pt surface begins to oxidize.

On Ag, oxygen reduction begins at -0.05V vs Pd/H and approaches a diffusion limited current density slightly greater than that of Pt. It is not possible to examine the possible existence of corresponding anodic peaks due to dissolution of the silver electrode, however the lack of an oxidation peak near the cathodic limit indicates silver is not active toward hydrogen oxidation.

Gold, like Ag, requires a relatively large overpotential for ORR with oxygen reduction starting at ca. +0.1V. The diffusion limited current density is also less than either Pt or Ag. And like silver, Au is not active towards hydrogen oxidation and no oxidation wave is observed for the protonation of triethylammine. However, a new product of oxygen reduction is observed as a second oxidation wave above 0.0V.

Palladium's absorption of hydrogen complicates its electrochemical behavior in protic electrolytes such as pILs. Oxygen reduction begins at approximately +0.2V vs Pd/H and the current rapidly increases, i.e. the activation limited region for ORR on Pd covers a much narrower potential space than that of ORR on Pt. The oxygen reduction current goes through a local maximum before settling at a similar diffusion limited rate to Pt. The cathodic stability of the pIL seems equivalent to that in the presence of Pt, and a broad oxidation wave is observe upon scanning positive of 0.0V vs Pd/H.

Unlike Pt however, reduction of the pIL cation does not form dihydrogen gas on a palladium electrode. Instead the reduced hydrogen is incorporated into the Pd, in the same way the Pd/H reference electrode is formed. Upon scanning positive this

Pd/H alloy can oxidize to reform triethylammonium, providing some deprotonated amine is local to the interface. At potentials greater than 0.0V vs Pd/H it also becomes possible to oxidize the hydrogen within the palladium to form triflic acid. Thus the oxidation wave above 0.0V is likely a convoluted mixture of hydrogen oxidation with the oxidation of ORR products.

RDE of ORR on Pt and Ag in TEATf

Figure 2.13 shows the anodic scans from cyclic voltammagrams of oxygen reduction on rotating disks of Pt and Ag in TEATf at room temperature. Inset within the plot containing RDE on Pt is a Levich plot for both the anodic and cathodic scan directions, while within the plot containing Ag is a Tafel plot showing the slope of 136mV/decade.

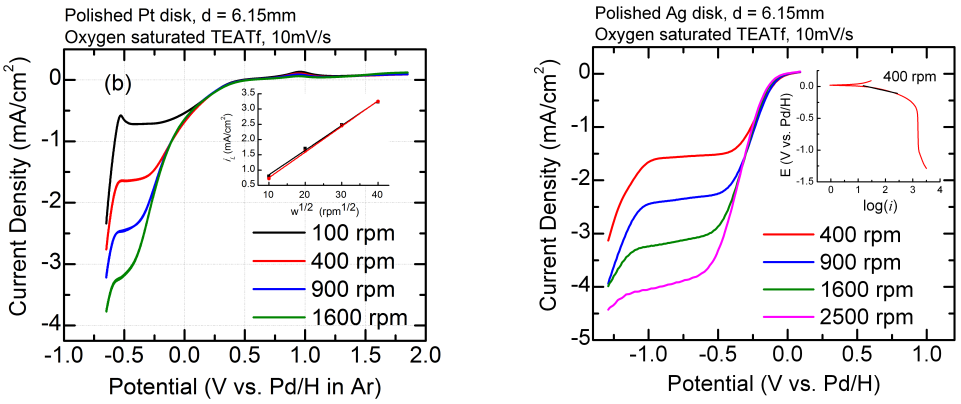

Figure 2.13: RDE of anodic scan on polycrystalline Pt and Ag at 10mV/s in O2 saturated TEATf at 25°C. Inset in the figure containing Pt is a Levich plot of limiting current vs rotation rate for both the anodic (red) and cathodic (black) scan directions. Inset in the figure containing Ag is a Tafel plot constructed from the 400rpm data with a slope of 136mV/decade. Data replotted from reference [61].

The hydrogen oxidation wave on Pt in Fig. 2.13 is muted relative to the CV in Fig. 2.12. This is due primarily to the less negative cathodic potential limit, but also a

result of the diffusion of dihydrogen away from the electrode. A small oxidation wave, common to both figures, is observed at approximately +0.75V. Unexpectedly, the activation region for oxygen reduction on Pt covers over a volt and the limiting currents used in the Levich plot must be taken from near -0.8V. The Levich slope on Pt is $82.4 \mu A cm^{-2} rpm^{-1/2}$.

In contrast to Pt, the activation region of silver covers a potential region approximately half as wide. This gives way to a broad mass transport limited region below -0.5V. The Levich slope for oxygen reduction on Ag in this region is in good agreement with that of Pt: $80.2 \mu A cm^{-2} rpm^{-1/2}$. This is in contrast with a marked difference in Tafel slopes, with Pt maintaining an 317mV/decade Tafel slope in the same current density region.

Diffusivity of Oxygen in TEATf

The solubility of oxygen in TEATf is 2.5mM, as determined gravimetrically. This is well in line with the potential oxygen content of other ILs (see table 2.1). With the oxygen solubility determined it is possible to eliminate an unknown from the Cottrell equation and use chronoamperometry to determine the oxygen diffusivity. Fig. 2.14 plots a chronoamperometric hold on Pt at -0.5V vs Pd/H in a static solution of oxygen saturated TEATf at room temperature.

The same data is plotted versus two different time scales in Fig. 2.14. Plotting the current versus $1/\sqrt{t}$ provides a more accurate evaluation of the quality of the fitted Cottrell equation through linearization. The inset plot shows the transient of the current with natural time. Fitting to the Cottrell equation (Eqn. 2.36) with an assumed 2.5mM oxygen concentration returned a net 2.86 electrons per O_2 molecule and $D_{O_2} = 20.11 \cdot 10^{-6} cm^2/s$.

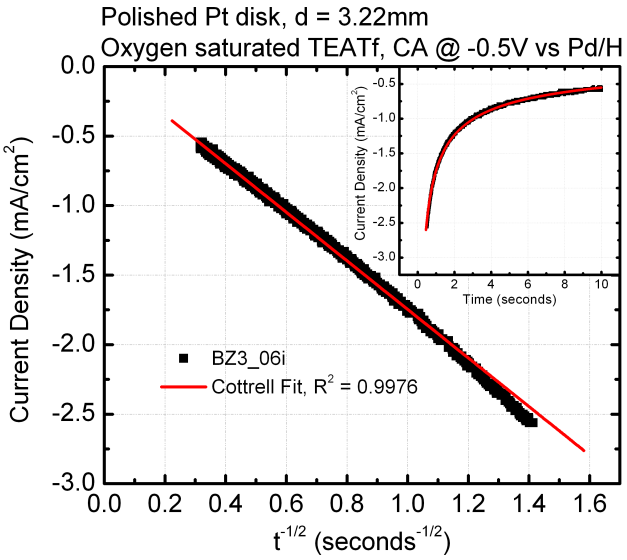

Figure 2.14: Chronoamperometric hold of Pt at -0.5V vs Pd/H in oxygen saturated TEATf at room temperature. Black is the raw data while the red line is a least squares fit to the Cottrell equation.

Mechanism of ORR in TEATf

Oxygen reduction on metals begins with adsorption of the oxygen molecule on the catalyst surface. Preventing this adsorption degrades the ability of a given catalyst to reduce oxygen. This is classically observed in the muted oxygen reduction currents on Pt in acids containing chloride anions [11], and shown in Ross' data (Fig. 2.8) where hydrogen adsorption prevents the full four electron reduction of dioxygen. Similarly, the presence of adsorbing species within pILs will have a strong effect on the degree and mechanism of oxygen reduction.

Oxygen reduction on silver in TEATf appears relatively clean and less affected by the problem of competitive adsorbates. Oxygen reduction begins at -0.05V vs Pd/H with a Tafel slope of 136mV/decade implying adsorbate coverage of similar blocking efficacy to that of hydroxide on Pt(110) in aqueous solutions [11] and a single

electron transfer in the rate limiting step. The activation limited region for ORR on Ag is fairly narrow and it is possible to make a clean Levich analysis made at many different potentials. Beyond the activation limited region, the Levich slope of mass transport limiting current can be solved to extract the total number of electrons transferred from Eqn. 2.47. Using the kinematic viscosity of $\nu = 0.469 cm^2/s$ from Belieres [95] and the diffusivity from the fitted data in Fig. 2.14, the Levich slope of $80.2 \mu A cm^{-2} rpm^{-1/2}$ corresponds to 1.97 electrons transferred per O_2 in the mass transport limited region.

Platinum has an almost identical Levich slope in the mass transport limited region which corresponds to 2.03 electrons per O_2. Thus oxygen reduction on Pt and Ag proceed to the same extent under mass transport limited conditions. This is in contrast to how the oxygen reduction begins on each metal. On silver, the activation limited region occupies a relatively narrow potential region compared to the approximate 1V spanned by the activation limited region on Pt. The Tafel slope of Pt is also much larger than that of silver: 317mV/decade vs 136mV/decade respectively.

Oxygen reduction on Pt is thus strongly limited by the rate of oxygen adsorption, rather than the electron transfer to form superoxide.

In sum, even though ORR proceeds to the same extent on both Pt and Ag, the rate limiting step on Pt is definitively Reaction 2.55, while Reactions 2.55 and 2.56 likely proceed at comparable rates on Ag. The first species formed in on both metals is superoxide.

$$O_2 \rightarrow O_2(ads) \tag{2.55}$$

$$O_2(ads) + e^- \rightarrow O_2^{\bullet -}(ads) \tag{2.56}$$

Superoxide irreversibly reacts with protons at such a rapid rate, that that the protonated form appears to have a pK_a of approximately 24 [34], even though $HO_2^\bullet$ has a measured pK_a of 4.69 in aqueous solutions [34; 40]. Given the lack of an efficiently reversible peak during ORR and the strong affinity of superoxide for protons, the deprotonation of the amine base according to reaction 2.57 is not implausible. The resulting free amine is likely the offending adsorbate which inhibits the adsorption of oxygen and its subsequent disproportionation. This adsorbed amine is probably the result of the oxidation wave observed at +0.7V vs Pd/H after oxygen reduction given its presence on all metals examined but palladium. It is possible for hydrogenated palladium to protonate the amine base, destroying it before the oxidation wave is observed.

$$O_2^{\bullet -}(ads) + BH^+ \rightarrow HO_2^\bullet(ads) + B \tag{2.57}$$

From perhydroxyl, both electrochemical and chemical mechanisms are available to complete the two electron reduction of oxygen for agreement with the Levich slopes.

$$HO_2^\bullet(ads) + e^- \rightarrow HO_2^-(ads) \tag{2.58}$$

$$HO_2^-(ads) + BH^+ \rightarrow H_2O_2 + B \tag{2.59}$$

and

$$HO_2^\bullet(ads) + HO_2^\bullet(ads) \rightarrow H_2O_2 + O_2 \tag{2.60}$$

In either case the net two electron reduction of oxygen to hydrogen peroxide is retained, though reaction 2.59 may occur to differing degrees dependent upon the

pK_a of the pIL cation relative to the H_2O_2 pK_a of 11.63. A complete four electron reduction of oxygen in pILs seems unattainable so long as the conjugate base of the cation is strongly adsorbing.

Summary of ORR in pILs

Oxygen reduction in pILs is analogous to ORR in buffered weakly acidic aqueous solutions with strongly adsorbing species insofar as the rate limiting step is adsorption of O_2 and the reaction does not proceed beyond two electrons per O_2. Unlike aqueous acid however, the pIL itself donates a proton during the reduction of oxygen and concurrently creates the offending adsorbate. Thus, the reaction scheme takes the form of:

$$O_2 \rightarrow O_2(ads)$$

$$O_2(ads) + e^- \rightarrow O_2^{\bullet -}(ads)$$

$$O_2^{\bullet -}(ads) + BH^+ \rightarrow HO_2^{\bullet}(ads) + B$$

followed by:

$$HO_2^{\bullet}(ads) + e^- \rightarrow HO_2^-(ads)$$

$$HO_2^-(ads) + BH^+ \rightarrow H_2O_2 + B$$

and

$$HO_2^{\bullet}(ads) + HO_2^{\bullet}(ads) \rightarrow H_2O_2 + O_2.$$

The amine base is the proposed species oxidized at +0.7V due to its persistence on all metals except hydrogenated palladium and its continued adsorption under RDE conditions on Pt. Rotating ring-disk experiments would further distinguish between hydrogen peroxide oxidation and amine oxidation, as well as investigate the degree

to which amine adsorption prohibits oxygen reduction by analysis of the kinetically limited current at different potentials.

2.5 Selection of an Aprotic Ionic Liquid

When adding protic sources, a number of considerations are important in selecting an IL from the many possible combinations of cations and anions. Foremost among these is the pK_a of the conjugate acid of the anion which effectively places an upper bound on the strength of acids that the IL can support, as protons from stronger acids would be captured by the anion. The Tf_2N anion is slightly preferable to triflate because its produces hydrophobic ILs with lower viscosities and lower melting points making it more convenient to work with. However its classification as a superacid with a pK_a lower than HTf is disputed [7; 60; 96].

Triflate and Tf_2N also have the advantage of extensive studies in the IL literature, including some work on oxygen reduction. They are non-interacting and stable during ORR [97; 98] because they frequently form ILs with low melting points. Further, Tf_2N has not been found to be specifically adsorbing, though there is some evidence for triflate adsorption on gold [99] at anodic potentials. Unfortunately, ionic liquids based on the Tf_2N anion are immiscible with water and since the effect of water on ORR is within the scope of this dissertation, the higher water contents afforded with triflate dictate the use of that anion.

It is also a requirement that cations not interact with superoxide or the electrode surface. A good first approximation for cations that do not react with superoxide are those which are relatively stable to alkaline conditions such as the tetraalkylammoniums. Di-substituted imidazoliums are not serviceable as the the proton on the C2 carbon is rapidly removed to form a carbene [100; 101]. This is evidenced

by the irreversible reduction of superoxide in C_4mimTf shown in Fig. 2.15a. By replacing the C2-proton with a methyl for 1-alkyl-2,3-dimethylimidazolium this decomposition is minimized. However, it is possible to protonate the imidazolium cation at the C4 or C5 position by HAl_2Cl_7 [102] and potentially other acids which may depress the effective pK_a's of extremely acidic donors.

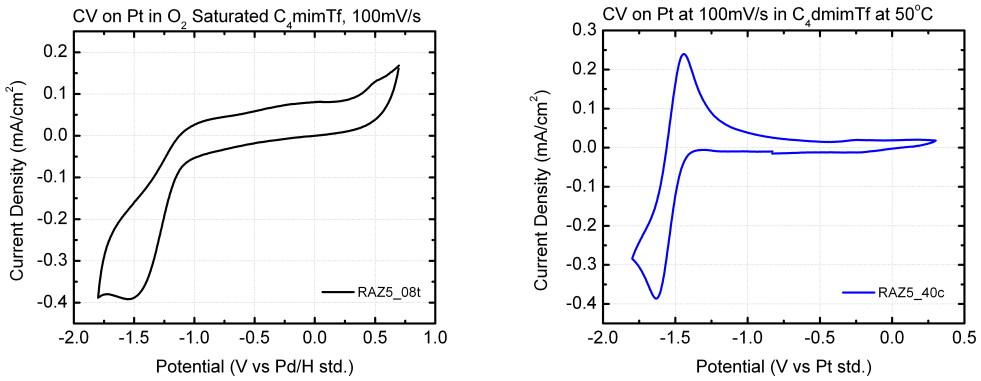

Figure 2.15: Cyclic voltammagrams in two closely related triflate ILs: (a) C_4mimTf and (b) C_4dmimTf. Scan rate of 100mV/s.

Synthesis of C_4dMImTf

1-butyl-2,3-dimethylimidazolium trifluoromethansulfonate was prepared according to previously published acid driven anion exchange procedures and dried before use. In a typical procedure, a solution of the imidazolium chloride was dissolved in a small amount of $18.3 M\Omega \cdot cm$ water – typically 1.2mL/gram – and chilled in an ice bath. A slight molar excess of chilled triflic acid was then added with stirring to the chloride solution. The graduated cylinder previously containing the triflic acid was then filled thrice with water to the same volume occupied by acid and emptied into the reaction mixture. Once the reaction mixture reached room temperature it was heated and water was removed by simple distillation at a pressure of < 100 mmHg

until the vigorous evolution of gas subsided. The pH of the distillate was tested and additional water equal to the approximate mass of the imidazolium chloride was added back to the reaction flask. The distillation was repeated five times or until the distillate tested above pH 6, indicating the removal of almost all HCl. The reaction flask now containing C_4dMImTf was purified by dissolving in approximately 5x the volume of dichloromethane and washing with ca. 0.5% by volume water until the the recovered aqueous layer did not precipitate AgCl upon treatment with 0.1M $AgNO_3$. Two additional washes upon failing to see precipitates completed the purification provided the tested pH neutral.

Chapter 3

EFFECT OF PROTON ACTIVITY ON THE MECHANISM OF OXYGEN REDUCTION

3.1 Introduction

The mechanism and pathways observed for the electrochemical reduction of oxygen are closely related to the strength and concentration of acidic species. Within aqueous solutions it is possible to observe the effect of proton activity over fifteen orders of magnitude, however two limitations exist. First, water is inherently protic with a $pK_a^{H_2O} = 15.7$ and has a concentration of 55.5M which makes it impossible to prevent the protonation of ORR products. And second, the formation of hydronium ($pK_a^{H_3O^+} = -1.7$) places an upper bound on the strength of acids that it is possible to investigate.

1-butyl-2,3-dimethylimidazolium triflate (C_4dMImTf) has neither of these shortcomings. In sufficiently dry solutions superoxide remains unprotonated and reversibly oxidized, while neither the cation nor anion are protonated except perhaps by the strongest known acids ($pK_a \lesssim -12$). Additionally, coverage of Pt surfaces by the hydroxyl species ($OH^{\bullet}(ads)$) is cited as one factor inhibiting oxygen reduction in aqueous solutions [24; 30; 31] and this can potentially be avoided by using non-aqueous electrolytes.

The mechanism of ORR is closely related to the availability of protons as outlined in Chapter 2.1. Examining the effect of protic additives in ionic liquids affords the rare opportunity to study superacids while maintaining low vapor pressures. In this chapter the extent of oxygen reduction is reported for a spectrum of acid pK_a's through a potential window spanning 2.5V.

3.2 Experimental

Materials

The ionic liquid C_4dMImTf was prepared by acid driven anion exchange as described in Section 2.5.

The acidic proton sources covering a wide range of pK_a's were made in a method similar that described for the creation of TEATf in Section 2.4. In a typical synthesis, 51 mmol of the conjugate base of the proton donor was dissolved in 10 mL of dichloromethane (DCM). To this solution, 50 mmol of triflic acid was slowly added. The large volume of dichloromethane relative to the amount of salt produced limited the need for active cooling; heat released by the reaction resulting in the boiling of DCM which prevented the temperature from climbing above ca. 50 according to a PTFE coated K-type thermocouple. Since yield was not important, the salt was removed from the dichloromethane by washing with a small volume of water. The resulting salt would preferentially solvate in the water with the neutral unreacted base remaining primarily in the DCM. This was confirmed by rotary evaporation of both the aqueous and DCM layer separately. A generally white crystalline powder would remain from the aqueous layer while the DCM residue typically resembled the original conjugate base. Table 3.1 lists the different proton sources and their respective pK_a's.

Methods

Oxygen solubility was determined gravimetrically by measuring the mass gain of a degassed 55mL sample upon saturation with oxygen. A 100mL round bottom flask was degassed under vacuum for five days prior to recording the initial mass. Immediately following, dry oxygen was purged through the solution for two days

Proton Source	$pK_a^{H_2O}$	pK_a^{DMSO}	Ref.
Triflic acid	-14	0.3	[7; 60; 103]
methanesulfonic acid	-2.6	1.6	[7; 103]
pyridinium triflate	5.21	12.33	[7; 104]
1,2-dimethylimidaozlium triflate	7.4	4-6	[103]
n,n-diethyl-n-methylammonium triflate	10.6	11	[7]
2-butyl-1,1,3,3-tetramethylguanidinium triflate	13.6	23.3[a]	[104]

[a] pK_a for tetramethylguanidinium in acetonitrile

Table 3.1: List of proton sources to be added to IL sorted by their aqueous pK_a.

to obtain the oxygen saturated mass. The mass of oxygen was confirmed by degassing the solution for one day to regain the initial mass. A photograph of this cell containing the 55mL of C_4dmimTf is shown in Fig. 3.1

In many ILs, the solubility of oxygen is ca. 3mM which gives guidance for the proton source concentrations needed for investigations. The protic additive titration commenced with 18mL of the dry neat C_4dMImTf in a glass RDE cell situated inside a MBraun glovebox ($<$1ppm H_2O) shown in Fig. 3.2. The water content was monitored via Karl-Fischer tritration (Mettler Toledo C20 Coulometric Titrator) and water content was consistently $<$0.1 mM H_2O. The ionic liquid was saturated with ultra-high purity Ar or O_2 via bubbling into the cell for at least 30 minutes piror to experiments at which point an Ar or O_2 overpressure was arranged. An aliquot providing 6mM of additive was added to reach approximately twice the oxygen concentration. This was followed by an addition to reach an intermediate value of 24 mM and then a large excess (100mM) of protons. At each concentration, a full rotating ring-disk (RRDE) analysis was performed for comparison across these concentrations and additives. The potentiostat was a Gamry Series G750. The RRDE experiments included both glassy carbon and platinum disk with

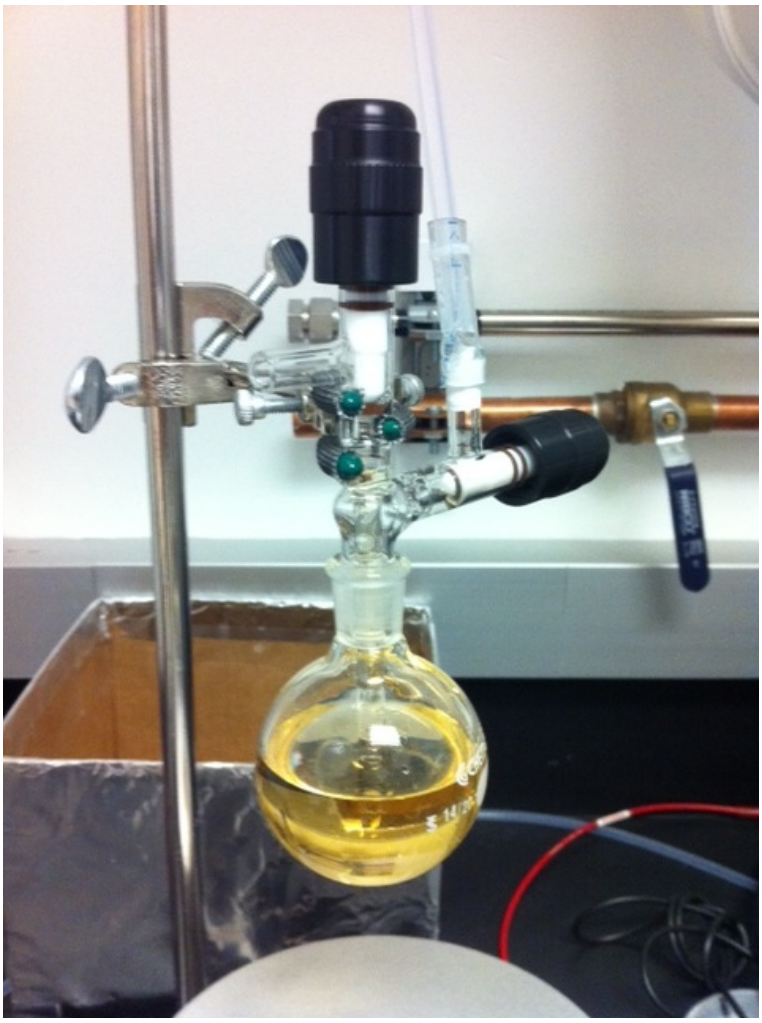

Figure 3.1: Photograph of of 100mL round bottom flask containing 55mL of C_4dmimTf and valve apparatus used for the gravimetric determination of oxygen solubility.

a Pt ring to collect product species. These disks were polished with 1μm alumina paste, washed with isopropanol and nanopure H_2O (>18 M-ohm resistivity). Viscosity changers were measured with a Rheosense m-Vroc viscometer to account for the effect in the RDE calculations (i.e. Levich equation). All experiments were performed at 50°C measured via a K-type thermocouple and stabilized by heating tape around the glass cell.

Figure 3.2: Photograph of RRDE cell for super acid titations. Cell is located in an M-Braun glove box with less than 0.1 ppm atmospheric water.

A quasi-reference electrode (Pt std. RE) was developed for these studies which consisted of an acid cleaned, H_2 flame annealed Pt wire situated in O_2-saturated neat C_4dMImTf solution. A Vicor porous glass frit sealed in PTFE housing separated this solution from the experiment volume. The reversible one electron electrochemical reduction of O_2 is observed at ca. -1.55V vs the Pt std. reference electrode which occurs at -0.31V vs. SHE and is pH-independent [23].

3.3 Results

ORR in Aprotic C_4dMImTf

Superoxide is stable and soluble in the studied ionic liquids as evidenced by the reversible one electron ORR process observed. Cyclic voltammograms of the reduction of dioxygen in aprotic C_4dMImTf on both platinum and glassy carbon RDE electrodes are shown in Fig. 3.3.

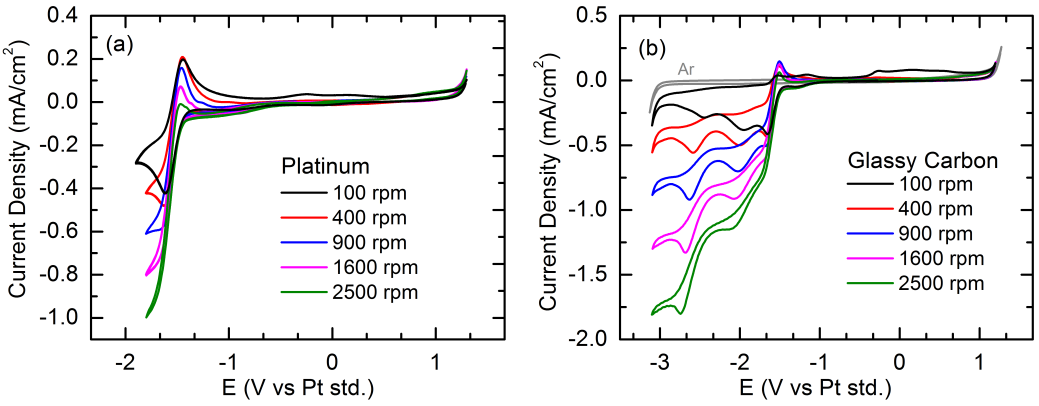

Figure 3.3: Cyclic voltammagrams at various rotation rates on (a) polycrystalline platinum and (b) glassy carbon in oxygen saturated C_4dMImTf at 50°C. Scan rate of 100mV/s.

In Fig. 3.3a, the reversibility of the one electron electrochemical reduction of O_2 is observed at -1.55V vs. the Pt std. reference electrode. as the rotation rate is increased, superoxide is convectively swept away from the Pt disk as indicated by the decrease in the anodic peak on the reverse scan. Identical behavior is observed for the glassy carbon electrode in terms of the $O_2/O_2^{\bullet -}$ redox couple when the negative potential limit is more anodic than -2.0V. If the potential is swept to more reducing potentials as in Fig. 3.3b, further reduction processes associated with oxygen are observed on glassy carbon. This is a familiar observation that has been associated with the further reduction of oxygen to the dianion O_2^{2-}.

ORR in the Presence of Protic Species

The RRDE experimental results of the triflic acid titration into C_4dMImTf are highlighted in the following section to act as a representative case for the identical titration experiments performed for all additives introduced in the experimental section. A selection of the electrochemical behavior and analysis upon the addition of triflic acid is shown in Fig. 3.4 for a Pt disk electrode.

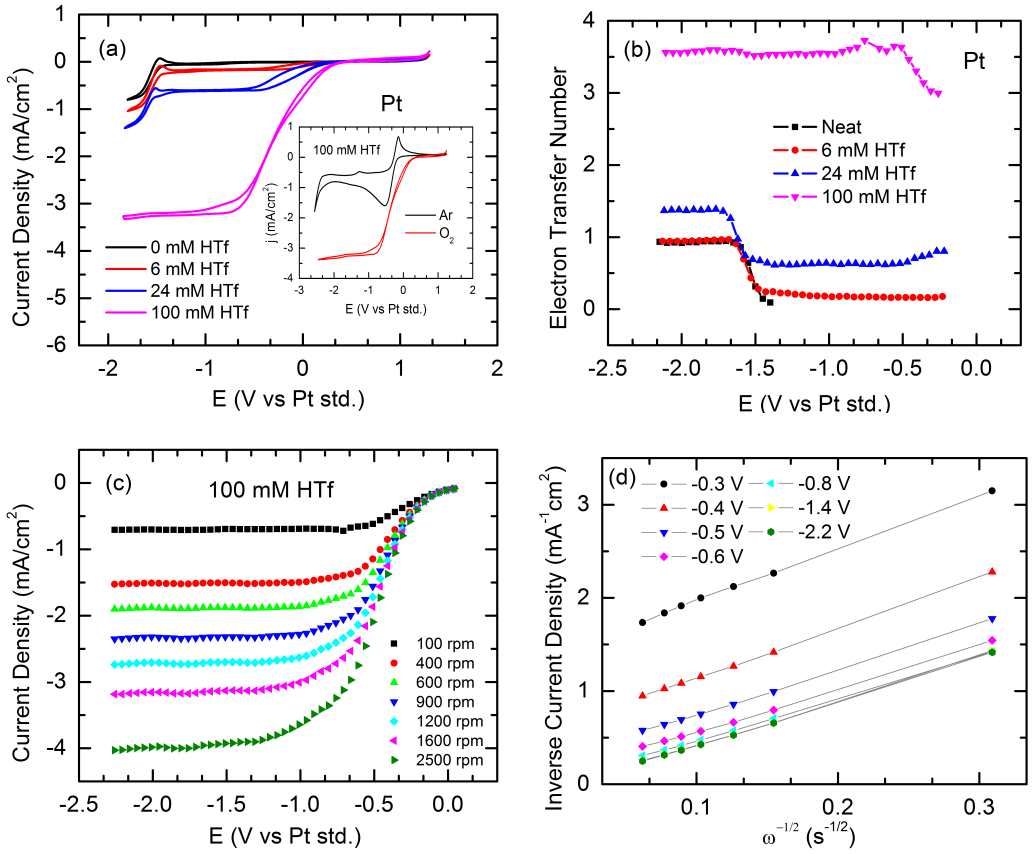

Figure 3.4: Oxygen reduction on a polycrystalline Pt rotating disk electrode in oxygen saturated C_4dMImTf at 50°C. (a) Cyclic voltammagrams at 100mV/s and 1600rpm for various triflic acid concentrations. (b) Number of electrons at each potential from the Kouteck-Levich slope in (d), which in turn is taken from the limiting current density plotted as a function of potential and rotation rate in (c).

The stepwise addition of triflic acid causes the O_2 reduction wave to increase in magnitude and the onset potential to shift positively as evidenced in Fig. 3.4a. This process is associated with the loss of superoxide reversibility (observed in the 0 mM HTf curve) due to superoxide protonation by triflic acid. Note that the addition of the strongly acidic HTf species increases the onset potential by ca. 1.8V. At the intermediate concentrations of 6 and 24 mM, two ORR waves are observed which illustrate the transition from superoxide production to a higher order ORR pathway which occurs at more positive potentials. The limiting current continues to grow with additive concentration until a maximum is reached. The number of electrons transfered in the ORR process throughout the course of the titration is plotted in Fig. 3.4b. In the absence of protic species, ORR is entirely a one electron process and gradually approaches the four electron process. The electron transfer number is determined from the steady-state chronoamperometric holds at numerous rotation rates as shown in Fig. 3.4c. The electron transfer number is determined from the slope of the Levich plot in the diffusion-limited regime. The intercept at the origin of the j^{-1} axis confirms that the current is entirely diffusion limited below -1.4V. The electron transfer number was determined from the Levich slope using the oxygen concentration of 2.5 mM (as determined gravimetrically) and diffusivity $D_{O_2} = 7.5 \cdot 10^{-6} cm^2/s$ as determined from the neat case where the reaction does not proceed beyond one electron.

Due to platinum's electrocatalytic properties for proton reduction, a hydrogen redox wave exists at ca. -0.3V as observed in the Ar and O_2 scans in the inset of Fig. 3.4a. In contrast, the glassy carbon electrode does not reduce the proton directly in the O_2 reduction regime as confirmed in the comparable experiments of Fig. 3.5.

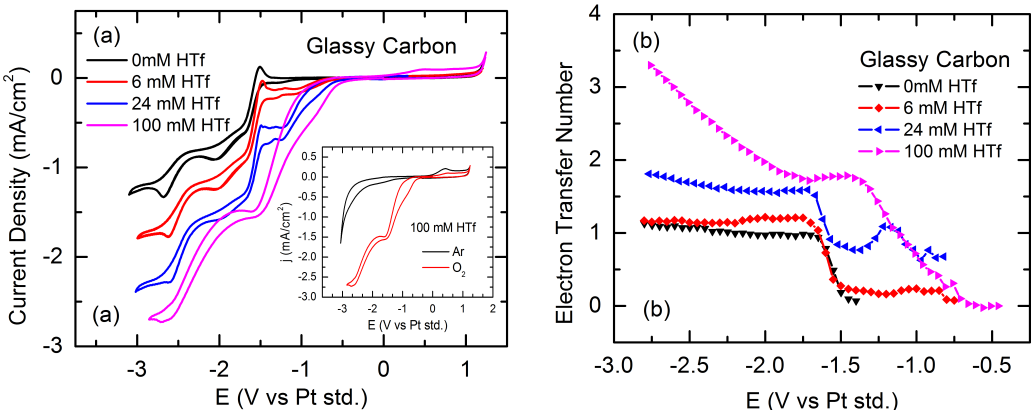

Figure 3.5: Oxygen reduction on a glassy carbon rotating disk electrode in oxygen saturated C_4dMImTf at 50°C. (a) Cyclic voltammagrams at 100mV/s and 1600rpm for various triflic acid concentrations, and (b) number of electrons at each potential from the Kouteck-Levich slope.

Although protons can be reduced on glassy carbon, much more negative potentials are required than on Pt as evidenced by the inset of Fig. 3.5a. The addition of the protic species causes an increase in the O_2 reduction pre-wave with an accompanied loss of superoxide reversibility as shown in the titration of Fig. 3.5a. At 100 mM HTf, the peak oxygen reduction current in the first reduction wave is approximately half of that for the Pt electrode case which reveals the effect of electrode material on extent of reaction. Determination of the electron transfer numbers plotted in Fig. 3.5b throughout the titration shows that the first ORR wave develops into a two electron process resulting in the formation of peroxide. As the potential is scanned more negatively, the reaction approaches a net four electron reduction. The formation of peroxide is confirmed by the RRDE data presented in Fig. 3.6.

Peroxide produced in the course of the ORR was detected at the ring by polarization at 1V at which peroxide oxidation proceeds as a diffusion limited process. Peroxide production was calculated from the ring-disk measurements according to Eqn. 3.1

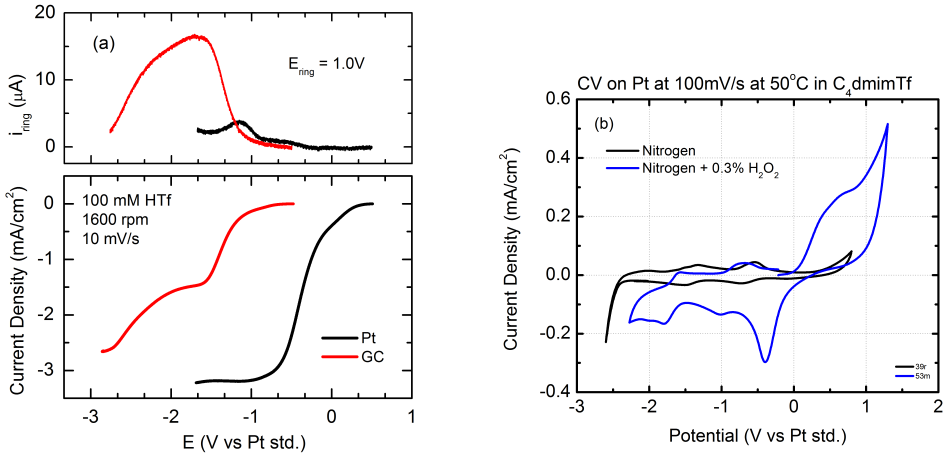

Figure 3.6: Hydrogen peroxide production on Pt and GC. (a) linear sweep voltammagram at 10mV/s in oxygen saturated C_4dMImTf at 50°C and 1600rpm with 100mM of triflic acid where the ring current shows oxidation of hydrogen peroxide, and (b) potential at which hydrogen peroxide is oxidized by the Pt ring.

where the collection efficiency N is 0.26 ± 0.05.

$$X_{H_2O_2} = 100 \cdot \frac{2 \cdot I_{ring}/N}{I_{disk} + I_{ring}/N} \tag{3.1}$$

For the glassy carbon disk electrode, the peak peroxide production measured is ca. 40% at -1.7V and initiates immediately upon ORR measured at the disk. In contrast, peroxide detection is delayed from the initiation of ORR by the Pt disk and only reaches ca. 5% at its maximum value occurring at -1.1V. These observations support the number of electrons transferred determined from the Levich slope analyses of Figures 3.4 and 3.5. Oxygen reduction proceeds mostly through the four electron pathway on Pt and is initially constrained to a two electron process on glassy carbon. As the glassy carbon disk is polarized more cathodically, a more complete reduction of oxygen to water is observed on during the second reduction wave. This is confirmed by the diminishing amount of peroxide detected at the ring

below -1.7V and by the increase in cathodic current.

To elucidate the effect of proton activity encompassing almost thirty orders of magnitude for both platinum and glassy carbon, identical titration experiments were performed for the additives introduced in Section 3.2. A compilation of the electron transfer numbers for all additives is shown in Fig. 3.7.

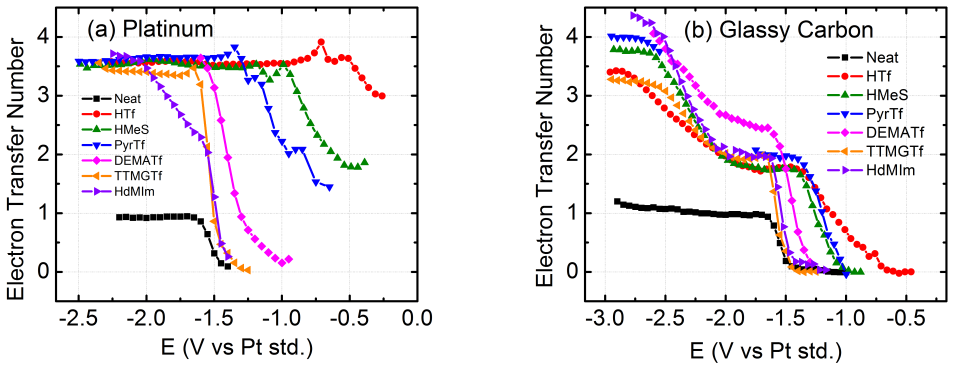

Figure 3.7: Number of electrons transfered as a influenced by pK_a over a 2.5V window for (a) Pt and (b) GC.

Fig. 3.7 demonstrates that ORR proceeds entirely through a one electron process in neat aprotic C_4dMImTf for both platinum and glassy carbon electrodes. It is evident from Fig. 3.7a that ORR approaches a four electron pathway regardless of the identity of the protic additive on Pt. From the glassy carbon plots in Fig. 3.7b, ORR is primarily a two electron process in the first reduction wave and gradually develops into the four electron pathway below -1.7V. Note that a portion of the pyridinium triflate data is neglected due to an impurity observed in the Ar scans. While the electron transfers numbers are relatively consistent across the full pK_a range of additives studied, the potentials at which these ORR processes commence exhibit a clear trend. An analysis of ORR onset potentials for a selection of additives investigated in Fig. 3.8.

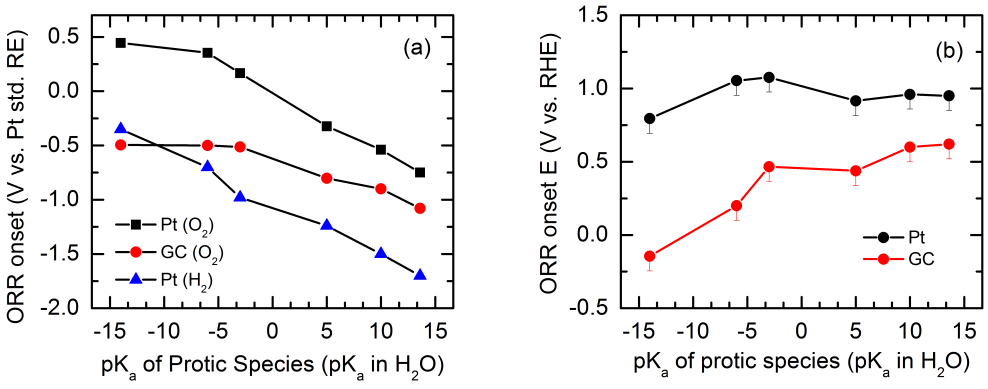

Figure 3.8: The turn-on potential for oxygen reduction on Pt and GC versus (a) the Pt std. reference electrode and (b) versus the potential of hydrogen evolution on Pt.

Oxygen reduction on both platinum and glassy carbon initiates at ca. -1.4V vs the Pt pseudo reference electrode in dry C_4dMImTf. On Pt, the addition of the strongly acidic HTf species increases the onset potential by ca. 1.8V. As the pK_a of the protic species increases from -14 to 13.6, the ORR onset potential decreases by approximately 50mV per decade change in aqueous K_a value. If the ORR onset potential is plotted versus the RHE reference electrode as in Fig. 3.8b, the majority of Pt ORR onset potentials are around 1V with the exception of the most acidic species. In fact, both Pt and GC onset potentials are lower than expected (assuming a 60 mV/decade change in proton activity) for HTf which suggests the effective pK_a for HTf in C_4dMImTf is higher than -14. This may be due to solvent leveling effects where the cation is acting as a buffer [102], however Thierry Robert et. al. found the pK_a of triflic acid in C_4mimTf to be less than that of HPF_6, HBF_4, and $HNTf_2$ [105] and so the aqueous pK_a may not be as applicable in this case. If the onset potentials in HTf solution are neglected in the linear regression, the slope becomes 60 mV/decade as expected.

3.4 Discussion

In aprotic ionic liquids, the addition of a proton source has a strong effect on the electrochemistry of oxygen reduction. The electrode and proton activity of the additive, expressed in the pK_a value, determines the ORR onset potential and extent of reaction. The ORR process in ILs involve the common rate limiting one electron reduction to superoxide as in aqueous solutions.

$$O_2(ads) + e^- \rightarrow O_2^{\bullet -}(ads) \tag{3.2}$$

In accordance with previous investigations, the superoxide redox potential is pH and electrode independent requiring only an electron source [11]. In the presence of a protic species, the one electron electrochemical step of Eqn. 3.2 is followed by chemical protonatoin of superoxide by the proton source (BH^+) to produce the perhydroxyl radical and base (B).

$$O_2^{\bullet -}(ads) + BH^+ \rightarrow HO_2^{\bullet}(ads) + B \tag{3.3}$$

From this point, a cascade of follow-up reactions regarding the perhydroxyl species occurs. It is possible for two perhydroxyl radicals to combine forming hydrogen peroxide and oxygen. Alternatively, a second electron transfer step to the perhydroxyl radical will produce the peroxidate anion (common to aqueous alkali) which can be further protonated to hydrogen peroxide (common to aqueous acid) depending on the pH of the solution since H_2O_2 has an aqueous pK_a of 11.63.

$$HO_2^{\bullet}(ads) + HO_2^{\bullet}(ads) \rightarrow H_2O_2 + O_2 \tag{3.4}$$

or

$$HO_2^{\bullet}(ads) + e^- \rightarrow HO_2^-(ads) \tag{3.5}$$

$$HO_2^-(ads) + BH^+ \rightarrow H_2O_2 + B \tag{3.6}$$

On Pt and some other electrodes, peroxide is decomposed catalytically and the liberated oxygen completes the net four electron reduction as sown in reaction 3.7. Glassy carbon, on the other hand, does not have any special propensity for peroxide disproportionation and the four electron reduction probably results from the electrochemical reduction of peroxide following Reaction 3.8.

$$2H_2O_2 \rightarrow O_2 + 2H_2O \tag{3.7}$$

or

$$H_2O_2 + e^- \rightarrow OH^- + OH^{\bullet}(ads) \tag{3.8}$$

$$OH^{\bullet}(ads) + e^- \rightarrow OH^-$$

$$2OH^- + 2H^+ \rightarrow 2H_2O \tag{3.9}$$

Unlike on Pt, the H_{ads} and O_{ads} species are not stabilized by the glassy carbon surface and the oxygen reduction process is limited to a two-electron stoichiometry in the first reduction step. Although protons can be reduced by glassy carbon, greater overpotentials are required than on Pt. These protentials are significantly more negative than the reduction potential for oxygen and initiate at potentials more cathodic than -1.7V at which point the four electron ORR reduction process occurs

on glassy carbon. However, on Pt there is a stronger interaction to reduce oxygen to water at low overpotential. This is the same case in aqueous systems [11].

It is well know that a ca. 60 mV/decade relationship exists between oxygen reduction potential and the term representing proton activity (see Section 2.1). In comparing the protic additives studied here, the pH term of Eqn. 2.2 is neglected given the equivalent concentration of protic species. Therefore, it is expected that the ORR potentials will shift by ca. 60 mV/dec change in effective pK_a. The tabulated pK_a values are measured in water or DMSO and therefore do not provide a truly accurate representation of the proton activity in the ionic liquid, however they do provide some basis to understand these systems. The observed shift of ca. 50 mV/dec change in pK_a is notable for its proximity to the theoretical value. At the extremely acidic end of the spectrum the observed onset potential for triflic acid was lower than expected based on its tabulated pK_a value. Its effective pK_a is therefore much lower which could be due to solvent levelling effects or protonation of the cation. Perhaps the aqueous pK_a value provides a more accurate representation of the effective pK_a value in ionic liquids than those tabulated for nonpolar DMSO due to the charged nature of ionic liquids. This is somewhat supported by the comparison of the guanadinium and malonate species which show similar ORR potentials and electron transfer numbers and have similar pK_a values in water while they have starkly contrasting pK_a in DMSO due to the charged or neutral nature of the two species.

This ORR behavior illustrates remarkable differences between ionic liquid and aqueous systems. The molar volume of water (55.5 M) is at least an order of magnitude larger than most ionic liquid systems and the steric properties imposed by the structure of the cationic proton donors are nontrivial compared to the aqueous

proton donor. These factors certainly affect the accessibility of the proton which permits the follow-up reactions to complete a four electron process. While at this time an analysis of the extent to which these effects manifest themselves is not completed, this work presents an indication of their existence.

3.5 Conclusions

The solubility of oxygen in C_4dMImTf is 2.5mM which permits the calculation of the diffusivity, $D_{O_2} = 7.44 \cdot 10^{-6} cm^2/s$ at 50°C, from the Cottrell equation. These values were used to determine the number of electrons transfered at any oxygen reducing potential for a spectrum of acidic additives.

Oxygen reduction in dry, aprotic C_4dMImTf cannot proceed beyond the reversible formation of superoxide without the addition of some acidic species. With the addition of strongly acidic protons, oxygen reduction on Pt is immediately promoted to a direct four electron reduction while glassy carbon sluggishly approaches two electron reduction followed by a separate region of four electron reduction. The addition of these protic species also shifts the potential at which oxygen reduction occurs in accordance with the Nernst equation based on the tabulated aqueous pK_a values.

Chapter 4

EFFECT OF WATER CONTENT ON THE MECHANISM OF OXYGEN REDUCTION

4.1 Introduction

Oxygen reduction cannot proceed beyond superoxide without some form of acid present, be it Lewis or Brönsted in nature [34]. When water is of order 55 Molar in concentration it is sufficiently abundant to protonate superoxide formed on platinum in alkaline solutions. Ionic liquids have intrinsically lower molar densities and are frequently touted for their hydrophobic nature. Thus the propensity of water to protonate superoxide in these exotic solvents can be reasonably questioned.

Distribution of Water in ILs

Water is termed the universal solvent for its polar properties and coordinating ability of many diverse ions. It also coordinates with itself leading to the phenomenon of surface tension. When ionic liquids were first studied in earnest in the early 1980s, they were unstable in the presence of water due to the very reactive anions they were made of. In the early 1990s, the first air and water stable ionic liquids were introduced and their hygroscopic nature noted [106]. The water within these structures was believed to coordinate mostly with the smaller and more charge dense anions (colloquially known as harder anions [107]). The cations of ionic liquids generally contain a high density of carbon and more diffuse charges giving them an intrinsically hydrophobic character.

A number of studies support this intuition and have provided some explanatory guidance. Cammarata et. al. performed an extensive survey of the molecular states

of water in ILs containing well known anions with cations based on butyl-methyl-imidazolium [108]. They concluded that the water generally exists in free state in the IL (not self-aggregated) and was hydrogen bonded to the anion. Triflate was among the anions compared and it was found to have a stronger H-bond acceptor capacity than either PF_6^- or BF_4^-, but not as strong as NO_3^- or $CF_3CO_2^-$. In fact, triflate was among the anions around which water does not self-aggregate and stronger hydrogen bonding anions can encouraged the formation of aggregated liquid water like regions. Cammarata also points out that the intense H-bonding of water with an anion makes the oxygen atom more basic which could inhibit its ability to protonate superoxide.

4.2 Experimental

Materials

1-butyl-2,3-dimethylimidazolium triflate was chosen for its miscibility with water. This series of experiments used ionic liquid from the same batch as the protic additive work in Chapter 3 and was made from the process described in Section 2.5.

Methods

C_4dMImTf melts near 40 so experiments were conducted at 50 ± 0.5. Temperature was controlled with a VWR 1157 recirculating chiller filled with a 60% ethylene glycol in water solution. The temperature was monitored via a K-type or J-type thermocouple. To observe the influence of small amounts of water, the temperature was held constant and the relative humidity (%RH) of the oxygen saturating gas or argon deaerating gas was controlled. An apparatus was constructed which diverted a controllable portion of regulated gas through a water aspirator. The humidified

gas was mixed in a tortuous chamber containing a Extech RH300 electrontic psychrometer before passing through a flow meter on its way to the RDE cell. Water content within the IL was sampled regularly using a minimum of $100\mu L$ and a Mettler Toledo C20 Coulometric Titrator.

Figure 4.1a show the humidity management system while Fig. 4.1b shows the RDE cell with IL. In the bottom left of the photograph is a Y-shaped junction connecting three short lengths of flexible tubing which supply gas to the cell. The flow of gas was adjusted to bubble up through the bottom of the solution past the counter electrode (red wire terminating in the PTFE plug) or maintained as an overpressure to maintain a contant %RH and oxygen content. The heating fluid supply line is located directly under the black thermocouple port facing the camera. Exiting from the rear of the cell is the gas exhaust tube which was bubbled through the hydrophobic IL N,N,N-trimethylethanolammonium bis(trifluorosulfonyl)imide.

The viscosity of the solution was recorded at temperature using a Rheosense m-Vroc viscometer for incorporation in the Levich equation. The temperature of the viscometer was maintained to 50 ± 0.1 using the same VWR 1157 recirculating chiller. Samples of IL solution were typically run at $15\mu L/min$ for 30 seconds and repeated six times at a given water content. The viscometer contained a dead volume of approximately $15\mu L$ and to prevent contamination between samples each one was chased with $100\mu L$ of methanol.

The potentiostats used were the Gamry Series G750 and Gamry Reference3000. RRDE experiments were conducted on both polycrystalline Pt and glassy carbon electrodes controlled by a Pine Instruments RRDE system. These disks were polished with 1μm alumina or diamond paste, washed with isopropanol and $18.3M\Omega \cdot cm$ water (Millipore's Milli-Q system).

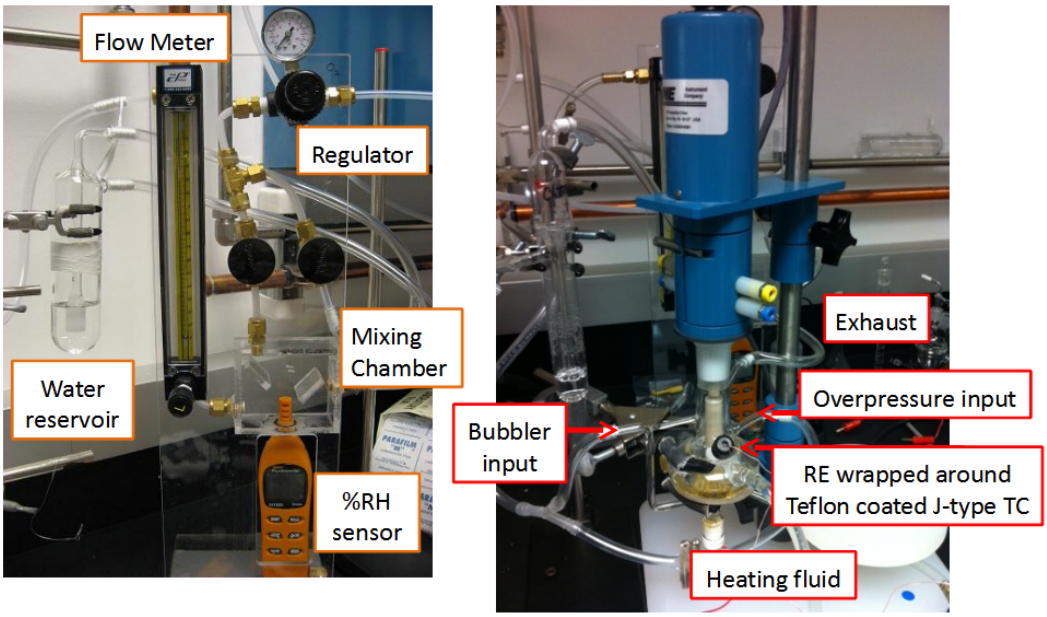

Figure 4.1: Photograph of RRDE cell for water titrations showing gas management, heating fluid circulation, and thermocouple.

A quasi-reference electrode (Pt std. RE) was developed for use C_4dMImTf which consisted of an acid cleaned, H_2 flame annealed Pt wire immersed in an O_2-saturated alliquot of C_4dMImTf. A Vicor glass frit sealed in PTFE housing separated the reference solution from the wet IL. Actual electrochemistry was performed relative to an immersed Pt wire in the water containing IL. This temporary reference wire was routinely checked against the standard Pt reference to prevent contamination of the standard with water.

4.3 Results

Superoxide is stable and soluble in ionic liquids as evidenced by the reversible one electron ORR reaction shown in Fig. 4.2. This figure shows the reduction of oxygen on both a rotating Pt electrode and rotating glassy carbon electrode. As the rotation rate is increased, superoxide is convectively swept away from the electrode

as indicated by the decrease in the anodic peak on the reverse scan.

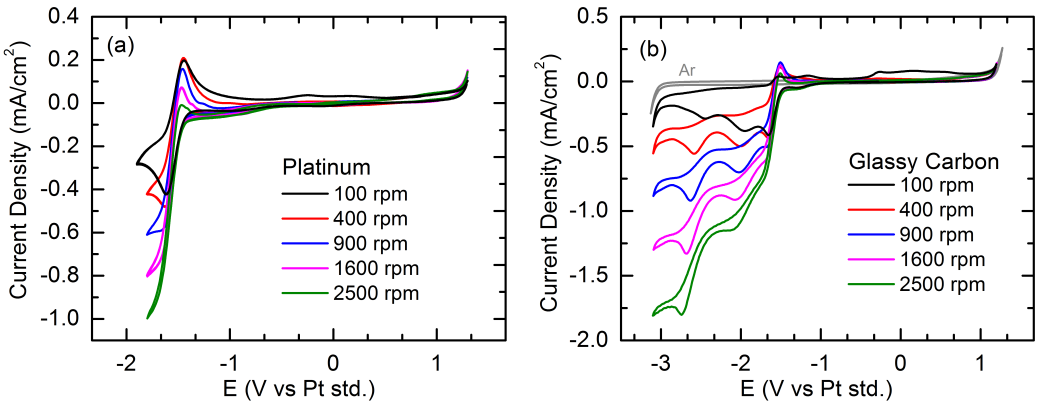

Figure 4.2: Cyclic voltammagrams at various rotation rates on (a) polycrystalline platinum and (b) glassy carbon in dry (¡0.1 mol%) oxygen saturated C_4dMImTf at 50°C. Scan rate of 100mV/s.

Titrating water into the IL by adjusting the relative humidity (%RH) of the oxygen allows for a tightly controlled water content. Surprisingly, the maximum water content attainable at 50 in C_4dMImTf was merely 16 mol% with 98%RH oxygen. This implies that even a water miscible IL like C_4dMImTf is extremely hydrophobic and have a severe positive deviation from Raoult's Law. These abnormally high solute vapor pressures are not uncommon for IL-water mixtures [109].

Fig. 4.3a shows a fit of the Cottrell equation (eqn 2.36) to a chronoamperometric hold at a diffusion limited potential for oxygen reduction on platinum with 0.4 mol% water. Three independent curves were recorded and the Cottrell equation was fit to their average. The concentration of oxygen was found to be 2.51 mM in close agreement with the gravimetric result of 2.49 mM. The electron transfer number is higher than expected, perhaps due to an inaccurate surface area or some convection within the IL volume. The chronoamperometric experiment was repeated at different water contents fit to a linear least squares regression shown in green in Fig. 4.3b.

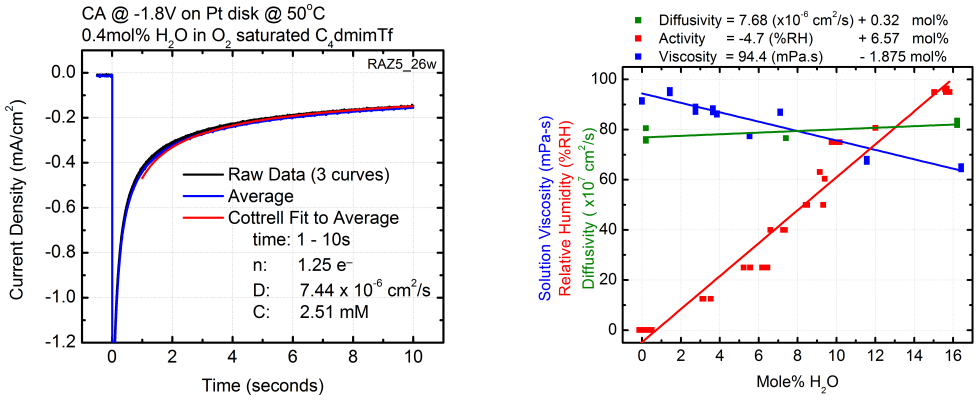

Figure 4.3: (a) Chronoamperometry of ORR on Pt fit to the Cottrell equation to find the oxygen diffusivity in dry C_4dMImTf. (b) Variation of diffusivity and viscosity with water content.

The average oxygen diffusivity in dry (<0.5mol% or <300ppm H_2O) C_4dMImTf was $7.68 \cdot 10^{-6} cm^2 s^{-1}$ and it increases slightly in response to the lower viscosity of higher water contents.

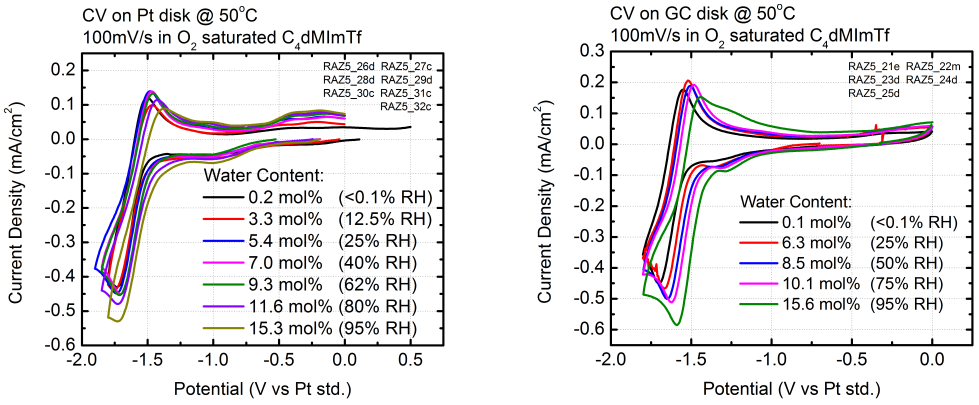

Figure 4.4: Cyclic voltammagrams of oxygen reduction in C_4dMImTF at 100mV/s and 50°C.

Fig. 4.4 shows cyclic voltammagrams attainable over the full range of %RH for the IL at 50°C for both Pt and glassy carbon. Superoxide oxidation diminishes

slightly at the highest water contents but still persists on the anodic sweep on both electrodes. A small oxidation wave at -0.5V begins to grow with increasing water content after reducing oxygen on Pt.

Fig. 4.5 shows linear sweep voltamagrams recorded in the rotating ring-disk geometry described in Section 2.3. The disk potential was swept cathodically at 10mV/s while maintaining the ring at -1.2V where superoxide would be oxidized. This slow scan rate combined with the relatively high rotation rate of 1600rpm ensures that the observed ring oxidation current correlates very closely with the disk potential. As the water content increases in Fig. 4.5 the onset potential for ORR increases and the overall current at any given potential also increases. The maximum disk current for any given water content is equivalent for both Pt and GC.

The oxidation of superoxide on the rotating ring turns on immediately with oxygen reduction and increases with increasing disk current except in the high water and strongly reducing potentials on glassy carbon. In this case the proportion of reduction current from the formation of superoxide diminishes as oxygen is further reduced to peroxidate. The additional electron involved in the reduction of oxygen is also observed in the almost doubling of the disk current at the highest water contents.

A series of chronoamperometric holds were performed at different rotation rates and potentials to produce Koutecky-Levich plots similar to the one shown in Fig. 4.6b. The potential was held constant at different potentials through the activation region of ORR on GC and the entire electrochemical window on Pt. Every thirty seconds the mass transport limiting current was noted and the rotation rate of the electrode increased. The inverse of the limiting current is plotted versus the inverse square root of the rotation rate to construct a Koutecky-Levich plot and extract

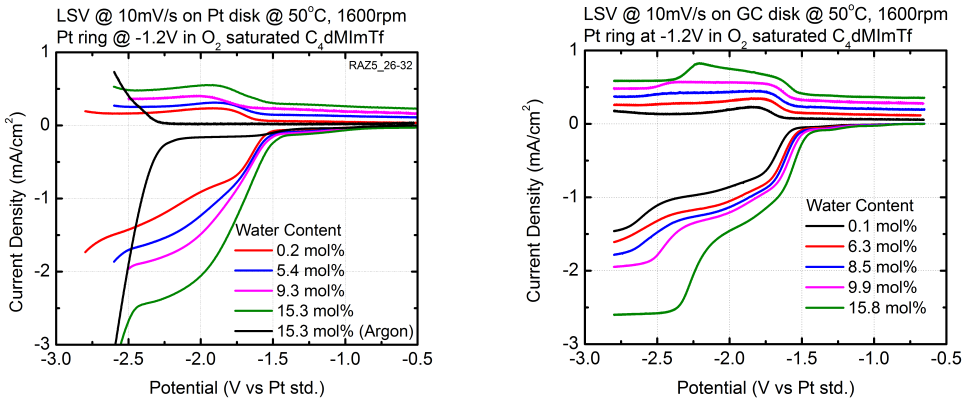

Figure 4.5: Linear sweep voltammagrams of oxygen reduction on rotating Pt and GC disks in C_4dMImTF at 10mV/s and 50°C. Ring oxidation current density is plotted above the disk reduction current and is shifted positive by $+100\mu A/cm^2$ for each water content.

the Levich factor (B-factor) from the slope of a linear fit. The B-factor contains information relating to the oxygen diffusivity, viscosity of the solution and total number of electrons transfered as discussed in Section 2.3.

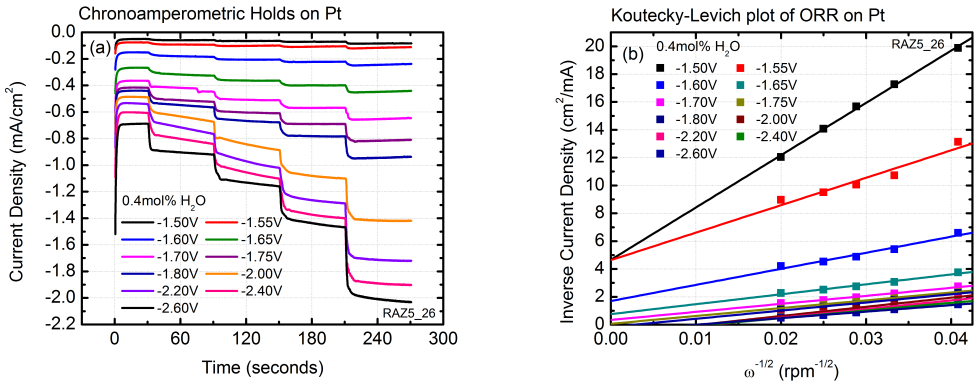

Figure 4.6: Chronoamperometric holds (a) converted to a Koutecky-Levich plot (b) for oxygen reduction on Pt in C_4dMImTF at 50°C.

A Koutecky-Levich analysis was performed over the full range of water contents on both Pt and GC. The slopes at various potentials and water contents are plotted

together in Fig. 4.7 for both Pt and GC. The B-factor increases with both potential and water content and the increase in turn-on potential from -1.5V to ca. -1.4V is clearly visible. The increase in the B-factor with more cathodic potentials at a given water content is only possible through an increase in the number of electrons transfered, however the increase in B-factor at a given potential in response to water content is convoluted with changes in diffusivity and viscosity. The significance of their contribution is accounted for and discussed in Section 4.4.

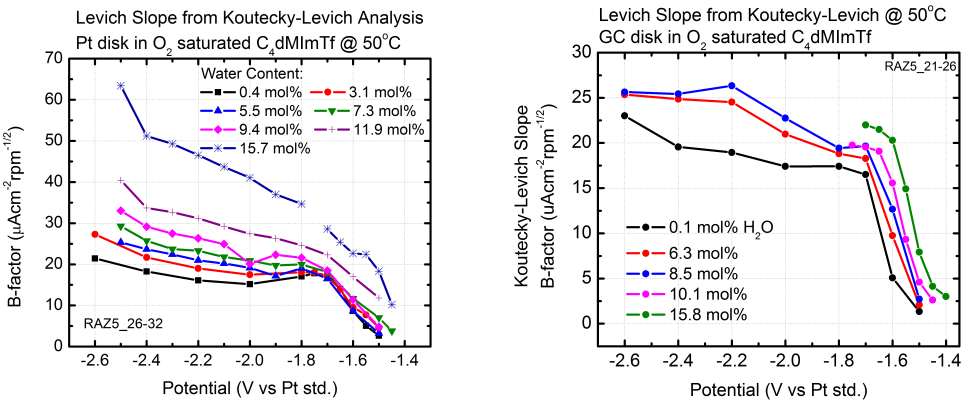

Figure 4.7: Levich slopes fit from mass transport corrected oxygen reduction currents at various potentials.

The turn-on potential for oxygen reduction was calculated from the linear sweep voltamagrams shown in Fig. 4.5. These curves were obtained under enhanced mass transport conditions which extends the activation limited region over a broader potential range. Linear fits were made of the current between $-0.3mA/cm^2$ and $-0.7mA/cm^2$ for both the anodic and cathodic sweeps and the zero current intercept was taken as the turn-on potential. These turn-on potentials are plotted for all curves and water contents in Fig. 4.8. Five of the six cathodic intercepts for Pt at 15.5mol% water were omitted from the linear fit to the data. Over the full range of water content the turn-on potential for ORR shifts by ca. 66mV and 118mV on Pt

and GC, respectively.

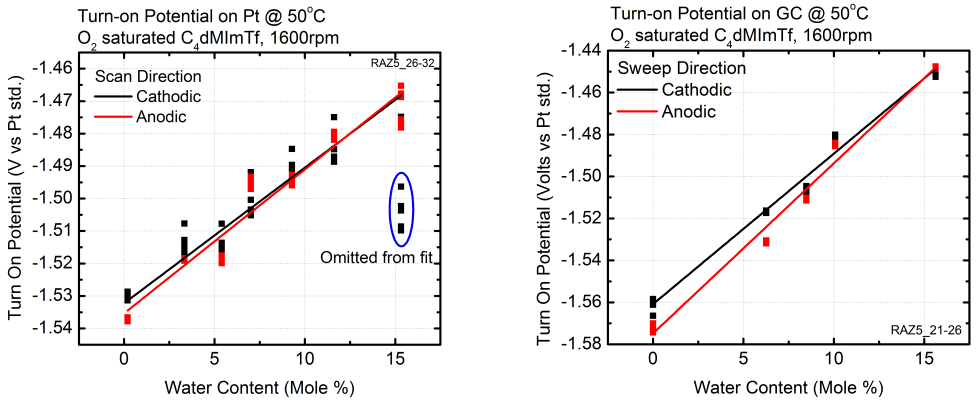

Figure 4.8: Turn-on potential for oxygen reduction taken from RDE linear sweeps. Encircled data points in the Pt case are not included in the linear fit.

Plotting the same data used to determine the turn on potential as potential vs log j permits the extraction of the Tafel slope as introduced in Section 2.3. The Tafel slope for each sweep direction and water content is plotted for both Pt and GC in Fig. 4.9. For a single electron limited process the theoretical Tafel slope is 120mV/decade. Values higher than 120mV/decade imply that the adsorption of oxygen and formation of superoxide is inhibited. This inhibition becomes stronger on both Pt and GC until the solution reaches 10mol% water, after which the Tafel slope is constant. Because both electrodes experience the same behavior the phenomenon impeding the formation of superoxide must be related to a solution side process.

To clarify the mechanism by which water would retard the formation of superoxide an understanding of the how electrode-IL interface changes with water content is necessary. One mechanism available to probe this interface is differential capacitance which provides the surface charge as a function of potential.

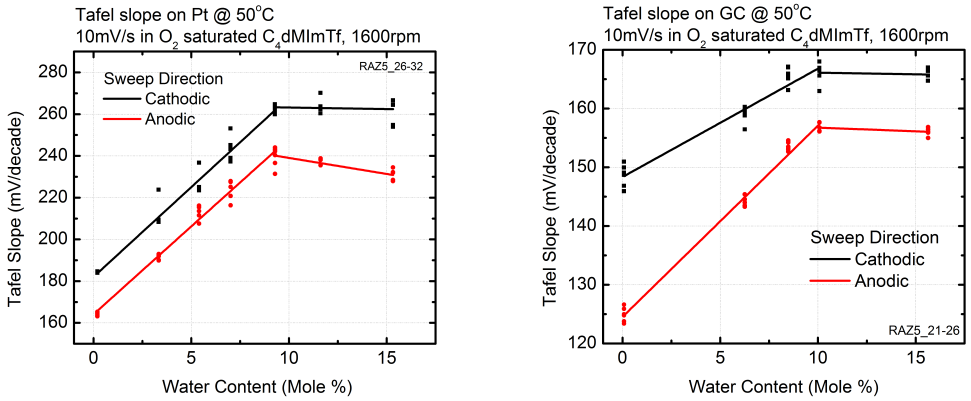

Figure 4.9: Tafel slopes of oxygen reduction on Pt and GC at each water content. Data taken from RDE linear sweeps.

Fig. 4.10 shows the differential capacitance curves for three water contents on both Pt and GC in deaerated C_4dMImTf at 50°C. The curves were obtained through a single frequency EIS technique taken at 200Hz and 10mV amplitude every 20mV through the electrochemical window. The water contents correspond with the dry, minimum Tafel slope case, an intermediate Tafel slope, and the fully saturated IL. The capacitance does not change appreciably with water content and there are no clear regions of adsorption. This implies that the offending species that inhibit the adsorption of oxygen and formation of superoxide are a product of oxygen and water since they are absent in the deaerated wet solutions.

4.4 Discussion

Extent of Oxygen Reduction

As in most dry aprotic electrolytes, oxygen reduction in dry C_4dMImTf begins with the formation of the superoxide species $O_2^{\bullet -}$ (eqn 4.2) as the rate limiting step. This occurs at approximately the same potential on both Pt and glassy carbon. In 1-butyl-

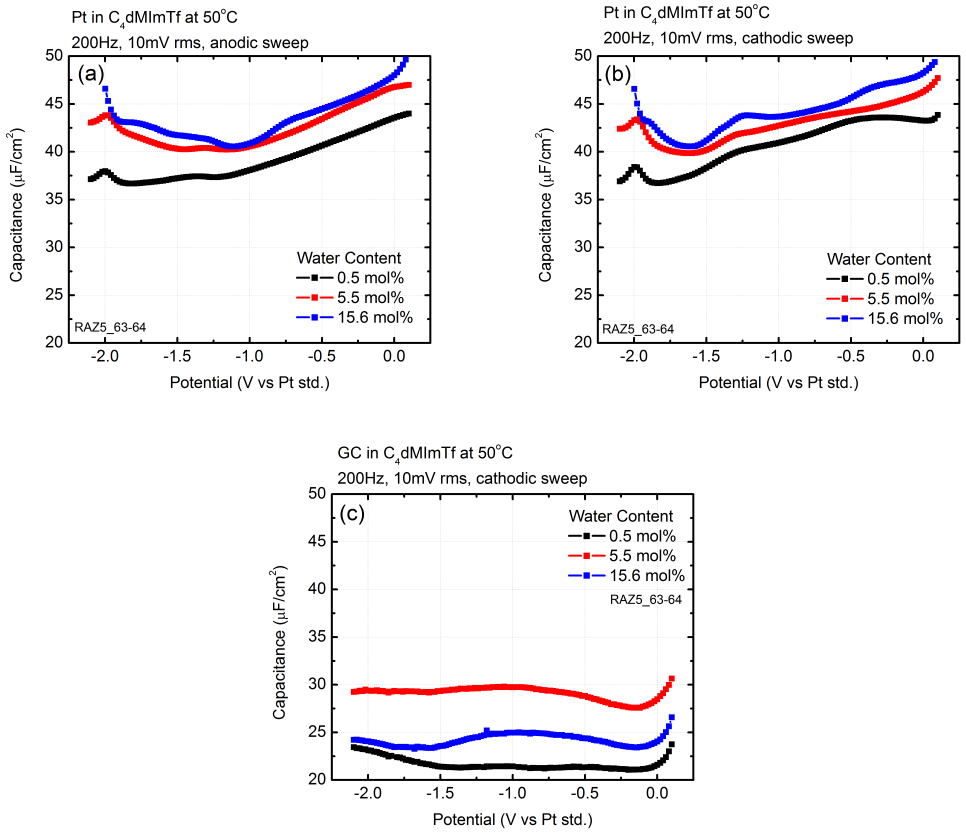

Figure 4.10: Differential Capacitance of GC and Pt electrodes in C_4dMImTf at 50°C. Recorded using single frequency electrochemical impedence spectroscopy at 200Hz and 10mV RMS in 20mV increments. (a) Shows the capacitance on Pt starting at -2.1V and stepping positive to +0.1V vs the Pt standard reference electrode, (b) stepping negative from +0.1V to -2.1V, and (c) for GC stepping cathodicall. Local maxima are present at $-1.35V \pm 0.02$ on Pt and $-0.80V \pm 0.02$ on GC.

2,3-dimethylimidazolium triflate, superoxide is soluble and it diffuses away from the electrode interface as evidenced by the diminished reversible oxidation wave under RDE conditions shown in Fig. 4.2.

$$O_2 \rightarrow O_2(ads) \tag{4.1}$$

$$O_2(ads) + e^- \rightarrow O_2^{\bullet -}(ads) \tag{4.2}$$

When acidic species are added to otherwise aprotic solvents oxygen reduction can proceed beyond the formation of superoxide [6] the details of which are discussed in Chapter 3. When water is sufficiently abundant, such as in aqueous alkaline solutions, it is an effective proton donor. This is due to superoxide's effective pK_a of ca. 24 [34]. With water acting as a proton source a second electron can reduce superoxide to the peroxidate species shown in Equation 4.3.

$$O_2^{\bullet -}(ads) + H_2O + e^- \rightarrow HO_2^-(ads) + OH^- \tag{4.3}$$

The completion of reaction 4.3 is followable by tracking the number of electrons transferred during the course of oxygen reduction. To arrive at the number of electrons transferred at any given potential, it is necessary to split the current into the components that are limited by the kinetics of the electron transfer and that are limited by the transport of reactants to the electrode surface. Koutecky's equation (eqn 4.4) does this stating the total current as the inverse sum of the kinetically limiting current i_k, and the mass transport limiting current i_L.

$$\frac{1}{i_{tot}} = \frac{1}{i_k} + \frac{1}{i_L} \tag{4.4}$$

term	description	value/unit
i_{tot}	total current	amps
i_k	kinetic current	amps
i_L	mass transport limited current	amps

Transport of the reactants to the electrode interface is limited by diffusion according to Equation 4.5.

$$i_L = \frac{nFAD}{\delta} C_o \tag{4.5}$$

term	description	value/unit
i_L	limiting current	amps
n	total electrons transferred	#
F	Faraday's constant	96485.3 C/mol
A	surface area	cm^2
D	diffusivity	cm^2/s
δ	diffusion layer thickness	cm
C_o	bulk concentration	$mole/cm^3$

The diffusion layer thickness is controlled by rotating the electrode where it becomes dependent upon the solution viscosity and rotation rate as derived by Levich for Equation 4.6 [110].

$$\delta = 1.61 D^{1/3} \nu^{1/6} \omega^{-1/2} \tag{4.6}$$

term	description	value/unit
δ	diffusion layer thickness	cm
D	diffusivity	cm^2/s
ν	kinematic viscosity	cm^2/s
ω	angular velocity	s^{-1}

Using the data collected for Fig. 4.3b, it is possible to account for the change in D_{O_2} and solution viscosity with water content. The concentration of oxygen in the IL/water mixture was assumed to follow Raoult's law as written in Equation 4.7, and the diffusivity and viscosity values were calculated for each water content based on the linear fit.

Combining equations 4.4 through 4.6 results in the Koutecky-Levich equation shown as Equation 4.8. The constant B-factor or Levich slope is the linear slope of the inverse current and a function of the solution properties and number of electrons transferred. Over the full range of water contents, the theoretical Levich slope

$$C_{tot}^{O_2} = C_{H_2O}^{O_2} \cdot X_{H_2O} + C_{IL}^{O_2} \cdot X_{IL} \tag{4.7}$$

term	description	value/unit
$C_{tot}^{O_2}$	concentration of oxygen in solution	mM
$C_i^{O_2}$	maxmimum solubility of oxygen in i^{th} component	mM
X_i	mole fraction of i^{th} component	$0.0 \leq X \leq 1.0$

ranges from 20 to 28 $\mu Amp \cdot cm^{-2} \cdot rpm^{-1/2}$. This theoretical Levich slope is used to extract the number of electrons transferred during oxygen reduction at each potential and such analysis is plotted in Fig. 4.11.

$$\begin{aligned} \frac{1}{i_{tot}} &= \frac{1}{i_k} + \frac{1}{0.62nFAD^{2/3}\nu^{-1/6}C_o\omega^{1/2}} \\ &= \frac{1}{i_k} + \frac{1}{B\omega^{1/2}} \end{aligned} \tag{4.8}$$

term	description	value/unit
i_{tot}	total current	amps
i_k	kinetic current	amps
n	total electrons transferred	#
F	Faraday's constant	96485.3 C/mol
A	surface area	cm^2
D	diffusivity	cm^2/s
C_o	bulk concentration	$mole/cm^3$
ω	angular velocity	s^{-1}
ν	kinematic viscosity	cm^2/s
B	Levich slope	$amps \cdot cm^{-2} \cdot s^{-1/2}$

As water becomes more abundant a greater proportion of oxygen is reduced with two electrons. This is clearly seen in Fig. 4.11 which is a revised version of Fig. 4.7 where the Levich slope has been converted to the number of electrons transferred.

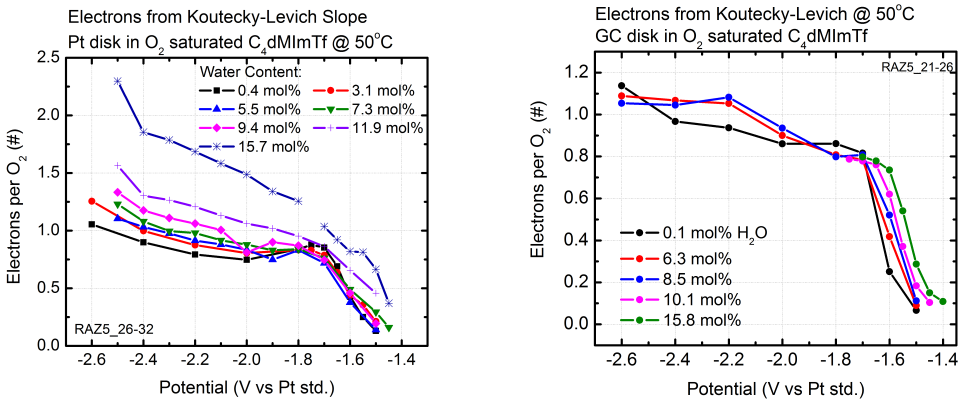

Figure 4.11: Electrons taken from the Levich slope of Fig. 4.7 after accounting for the change in viscosity, diffusivity, and solubility of oxygen with increasing water content.

Water Inhibited Adsorption of Oxygen

While additional water enables the protonation and further reduction of superoxide to form the peroxidate species according to Reaction 4.9, the excess water also leads to the inhibited adsorption of dioxygen as evidenced by the increase in Tafel slope plotted in Fig. 4.9.

$$O_2^{\bullet -}(ads) + H_2O + e^- \rightarrow HO_2^-(ads) + OH^- \tag{4.9}$$

The origin of this initially sluggish reduction is uncertain. The structure of the electrochemical double layer (Fig. 4.10) does not appear to change appreciably with water content and this is corroborated by the finding that water has little effect on bulk IL structure until the composition exceeds 50mol% [111]. Compton et al. observed a surprisingly strong interaction between the superoxide anion and the C_4dmim^+ cation in the popular ionic liquid $C_4dmimTf_2N$ [55]. This result is reproduced in dry $C_4dmimTf$ in Fig. 4.12.

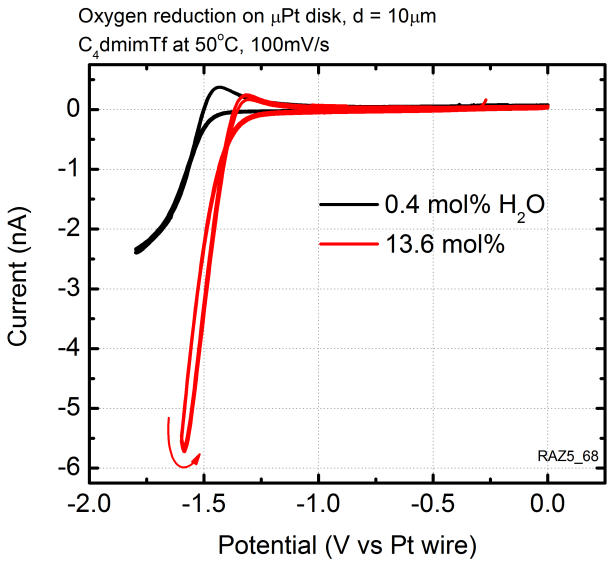

Figure 4.12: Cyclic voltammagram at 100mV/s on μPt at two different water contents. Potentials versus an immersed Pt wire.

The remarkably short diffusion distances afforded by a small electrode permit the rapid approach of oxygen and water to the platinum surface and the rapid egress of products away from the electrode. The existence of a return oxidation wave is uncommon on micro electrodes and implies that the products are very slow diffusers. This behavior is repeated at high water contents, but the cyclic voltammagram also crosses over itself, a feature present due to the further reduction of superoxide. The oxidation of peroxidate, which is expected at -0.5V vs Pt and is seen in Fig. 4.4, is absent on the micro electrode. This means that peroxidate is a much faster diffuser than superoxide in C_4dmim^+ based ILs and is not a species inhibiting the adsorption of O_2.

The remaining product of oxygen and water which could inhibit further oxygen adsorption is hydroxide. Hydroxide adsorption itself is unlikely on Pt at potentials this cathodic, but it is possible that the IL is unstable in the presence of hydroxide

at these temperatures and the products of their reaction inhibit ORR. A possible reaction is the deprotonation of the C2 methyl [112].

Origin of Potential Shift with Water

As the water content of the IL is increased so too does the potential at which oxygen reduction begins. This effect is visible in almost every figure of this chapter but is plotted explicitly in Fig. 4.8. The shift in turn on potential for Pt is ca. 66mV over the full range of water content, while the corresponding shift on GC is ca. 118mV. All of these shifts are versus the Pt standard reference electrode with a approximately constant internal water content and were confirmed with separate reference electrodes.

On platinum, the reduction of oxygen with sufficient water proceeds through the following reaction for which a corresponding form of the Nernst equation is written:

$$O_2 + H_2O + 2e^- \leftrightarrow HO_2^- + OH^- \tag{4.10}$$

$$\begin{aligned} E &= E^o - \frac{RT}{nF}\ln\frac{[HO_2^-][OH^-]}{[H_2O]\cdot P_{O_2}} \\ &= E^o - \frac{RT}{nF}\ln\frac{[H^+][OH^-]}{[H_2O]} - \frac{RT}{nF}\ln\frac{[HO_2^-]}{P_{O_2}} \\ &= E^o - \frac{RT}{nF}\ln\frac{K_w}{[H_2O]} - \frac{RT}{nF}\ln\frac{[HO_2^-]}{P_{O_2}} \\ &= E^o - 0.0295\cdot\log K_w + 0.0295\cdot\log[H_2O] - 0.0295\cdot\log\frac{[HO_2^-]}{P_{O_2}} \\ &= E^o + 0.0295\cdot pK_w + 0.0295\cdot\log[H_2O] - 0.0295\cdot\log\frac{[HO_2^-]}{P_{O_2}}. \end{aligned} \tag{4.11}$$

Rearranging Equation 4.11 the self-ionization constant of water is separated from its concentration. In the final form of the Nernst equation for reaction 4.10 it becomes clear that the oxygen reduction potential shifts by ca. 30mV per decade

change in water concentration providing $\log \frac{[HO_2^-]}{P_{O_2}}$ stays constant. In the course of the RRDE experiments, the water content varied from ca. 0.1mol% (approximately 4.7mM) to 15.6mol% (approximately 860mM), a span of just over two decades. This results in a predicted increase of 66.7mV in the oxygen reduction potential which agrees perfectly with the observed 66mV shift on Pt.

On glassy carbon the shift in the oxygen reduction potential is more sensitive to water, implying that a different reaction with one electron per water molecule sets the potential. Such a reaction, of which reaction 4.12 is a plausible candidate, would correspond to a potential shift of 134mV across the full range of water contents while the observed shift is ca. 118mV. This reaction has been observed on GC electrodes in DMF and ACN with high water contents [36; 37; 113].

$$O_2 + H_2O + e^- \rightarrow HO_2^\bullet + OH^- \tag{4.12}$$

The existence of two separate reactions determining the response of oxygen reduction to water is unsurprising in light of Fig. 4.5. Oxygen is reduced directly with two electrons on Pt while there are clearly two distinct reduction reactions occurring on GC. The first reduction wave on GC could be due to reaction 4.12 while the second wave, which begins at ca. -2.0V in the high water case, could be the reduction of the perhydroxyl radical species.

4.5 Conclusions

The ionic liquid chosen for these water experiments, C_4dMImTf, is miscible with water but surprisingly hydrophobic. At 50°C, water is rejected from the solution into highly humidified air until the solution reaches approximately 16mol% water.

When one sixth of the solution components are water molecules, the viscosity decreases appreciably which increases the diffusivity of oxygen. The solubility of oxygen within the solution also decreases slightly with additional water.

As in all previously investigated aprotic solvents, oxygen reduction in ionic liquids begins with the rate limiting one electron formation of superoxide as written in reaction 4.14. Superoxide strongly associates with the C_4dMIm^+ as evidenced by its much reduced diffusivity compared to dioxygen.

$$O_2 \rightarrow O_2(ads) \tag{4.13}$$

$$O_2(ads) + e^- \rightarrow O_2^{\bullet -}(ads) \tag{4.14}$$

With sufficient water, superoxide is protonated to form the perhydroxyl radical according to reaction 4.15. However, unlike the the results of Chapter 3, 100mM water is insufficient to drive this reaction to an appreciable degree.

$$O_2^{\bullet -}(ads) + H_2O \rightarrow HO_2^{\bullet} + OH^- \tag{4.15}$$

As the water content increases and the hydroxide produced according to reaction 4.15 becomes more abundant, the Tafel slope increases to a limiting value corresponding to inhibited adsorption of oxygen. It is suggested that adsorption is inhibited by a reaction between the hydroxide and the C_4dMIm^+ cation at these elevated temperatures and not by the interaction of C_4dMIm^+ with superoxide or peroxidate, or by changes in the structure of the double layer.

On platinum, reaction 4.15 is rapidly followed by the reduction of the perhydroxyl radical according to reaction 4.16.

$$HO_2^{\bullet} + e^- \rightarrow HO_2^- \tag{4.16}$$

However this final reaction is sluggish on glassy carbon and thus the potential at which oxygen is reduced on GC is more sensitive to the water content of the IL. The different controlling reactions on Pt and GC comport with the differential capacitance results in suggesting there is no water-rich layer at the electrole—IL interface.

In summary, oxygen reduction can proceed through two electrons in wet C_4dMImTf but not further to four electrons. The reduction does not progress beyond superoxide if there is insufficient water present.

Chapter 5

SUMMARY AND FUTURE OPPORTUNITIES

This thesis presented the mechanisms of oxygen reduction in two ionic liquids under a variety of conditions. By way of introduction (Chapter 2.4), a selection of experiments performed by Lei Tang et. al. [61] in triethylammonium triflate (TEATf) were analyzed and the mechanism of oxygen reduction deduced. TEATf is an inherently protic ionic liquid and its electrochemical behavior closely mimics that of water. Next, protons of different pK_a's were titrated into the inherently aprotic ionic liquid 1-butyl-2,3-dimethylimidazolium triflate (C_4dMImTf) and the mechanism of oxygen reduction was tracked as a function of acid pK_a and potential (Chapter 3). Finally, water was used as the proton donor for ORR in C_4dMImTf as part of an attempt to mimic alkaline water conditions, and an account of the different mechanisms on Pt and GC was given (Chapter 4).

5.1 Protic Ionic Liquids: TEATf

In TEATf oxygen is soluble to 2.5mM and its diffusivity is very similar to that of water at $D_{O_2} = 20.11 \cdot 10^{-6} cm^2/s$. These values were used in a Koutecky-Levich analysis to determine the mechanism of oxygen reduction on Pt and Ag. Oxygen reduction was found to follow the generic mechanism below where BH^+ represents the triethylammonium cation.

$$O_2 \rightarrow O_2(ads)$$

$$O_2(ads) + e^- \rightarrow O_2^{\bullet -}(ads)$$

$$O_2^{\bullet -}(ads) + BH^+ \rightarrow HO_2^{\bullet}(ads) + B$$

followed by:

$$HO_2^{\bullet}(ads) + e^- \rightarrow HO_2^-(ads)$$

$$HO_2^-(ads) + BH^+ \rightarrow H_2O_2 + B$$

and

$$HO_2^{\bullet}(ads) + HO_2^{\bullet}(ads) \rightarrow H_2O_2 + O_2$$

Through cyclic voltammetry on a variety of metals, the amine based was determined to strongly adsorb on the noble metal surfaces of Au, Pt and Pd electrodes and inhibit the adsorption of oxygen. This inhibited oxygen adsorption was not observed on Ag. None the less, oxygen reduction was limited to two electrons on each metal investigated and this could be reasonably attributed to the free amine base preventing the disproportionation of hydroxide.

An investigation using a pIL cation of similar pK_a but which deprotonates to form a less strongly adsorbing species would be an illuminating addition to this work.

5.2 Acid Titration into Aprotic IL, C_4dMImTf

Proton sources of different pK_a's were titrated into C_4dMImTf up to a concentration of 100mM and their effects on the mechanism of oxygen reduction were observed. The mechanism of oxygen reduction in aprotic ILs begins with the formation of superoxide, as it does in all solvents. The superoxide is rapidly protonated and the resulting perhydroxyl species is reduced to peroxidate. Peroxidate's conjugate acid has an aqueous pK_a of ca. 11.7 and is also protonated by the excess acid to form hydrogen peroxide.

$$O_2 \rightarrow O_2(ads)$$

$$O_2(ads) + e^- \rightarrow O_2^{\bullet -}(ads)$$

$$O_2^{\bullet -}(ads) + HA \rightarrow HO_2^{\bullet}(ads) + A^-$$

$$HO_2^{\bullet}(ads) + e^- \rightarrow HO_2^-(ads)$$

$$HO_2^- + HA \rightarrow H_2O_2 + A^-$$

From the formation of peroxide, the mechanisms on Pt and GC diverge. On a clean Pt surface, peroxide is rapidly disproportionated into water an oxygen completing the four electron reduction. Glassy carbon in contrast has no special propensity for peroxide disproportionation and the completion of the four electron reduction requires further reducing potentials.

$$2H_2O_2 \rightarrow O_2 + 2H_2O$$

$$or$$

$$H_2O_2 + e^- \rightarrow OH^- + OH^{\bullet}(ads)$$

$$OH^{\bullet}(ads) + e^- \rightarrow OH^-$$

$$2OH^- + 2H^+ \rightarrow 2H_2O$$

The potential at which oxygen reduction occurs shifts with pK_a as predicted by the Nernst equation which confirms the applicability of the proton donor's aqueous pK_a values. However, triflic acid appears less acidic than predicted, perhaps due to solvent leveling effects, protonation of the C_4dMIm^+ cation, or simply an inaccurate aqueous pK_a value.

To clarify why oxygen reduction is less responsive to the extremely acidic end of the pK_a spectrum, similar experiments could be performed in ILs with different anions such as PF_6^-, BF_4^-, and Tf_2N^-. ILs composed of Tf_2N^- anions have the additional bonus of being liquid at room temperature which would permit a wide range of temperatures to be easily investigated.

5.3 ORR in Wet C_4dMImTf

Water as a proton donor was originally intended to be included in the pK_a titration work of Chapter 3, but the persistence of superoxide at 100mM H_2O required titrating to higher concentrations which altered the physicochemical properties of the IL. Water was added to C_4dMImTf up to a concentration of 15.8mol% (approximately 870mM) which required accounting for the decrease in viscosity and oxygen solublity, and the increase in oxygen diffusivity.

As the water content increases, the number of electrons transfered during ORR increases to a maximum of two during the formation of peroxidate. Higher water contents up to 10mol% also corresponds with an increase in the Tafel slope, i.e. a decrease in the oxygen adsorption rate. Above 10mol% water the Tafel slope was found to be constant. This was theorized to be due to a change in the double layer structure where water was expected to be excluded to the electrode interface by the hydrophobic IL, however no appreciable change in the deaerated double layer capacitance was found while increasing the water content. This implies that the inhibited adsorption of O_2 results from a reaction between O_2 and water, likely caused by the hydroxide released during superoxide protonation.

The turn-on potential for oxygen reduction increased with water content in a Nernstian fashion, however the sensitivity of ORR to water was electrode dependent with

GC being more sensitive. Two controlling reactions were proposed to explain the difference in the Nernstian potential on Pt and GC.

Oxygen reduction on Pt in the presence of water is proposed to follow the following direct two electron mechanism:

$$O_2 + H_2O + 2e^- \leftrightarrow HO_2^- + OH^-$$

While on glassy carbon the ratio between water and electrons was found to be unity, resulting in the conclusion that it proceeds through the following reaction and that the adsorbate implied by the increase in Tafel slope inhibits the reaction of two perhyroxyl radicals to form hydrogen peroxide [36; 37; 113].

$$O_2 + H_2O + e^- \rightarrow HO_2^{\bullet} + OH^-$$

The distribution and basicity of water in ILs is tied to the hydrogen bonding ability of the anion. Triflate is known to have a moderate hydrogen bonding propensity in ionic liquids [108] and further investigation using the PF_6^- anion, which has very little H-bonding ability, and $CF_2CO_2^-$, which has a great capacity for hydrogen bonding, could prove more illuminating.

[1] A. V. Anantaraman and C. L. Gardner, "Studies on ion-exchange membranes. Part 1. Effect of humidity on the conductivity of Nafion," *Journal of Electroanalytical Chemistry*, 1996.

[2] J. J. Xu, H. Ye, and J. Huang, "Novel zinc ion conducting polymer gel electrolytes based on ionic liquids," *Electrochemistry Communications*, vol. 7, pp. 1309–1317, 2005.

[3] P. J. Dyson and T. J. Geldbach, "Applications of Ionic Liquids in Synthesis and Catalysis," *Interface*, vol. 16, no. 1, pp. 50–53, 2007.

[4] M. J. Earle, J. M. S. S. Esperanca, M. A. Gilea, J. N. Conogia, L. P. N. Rebelo, J. W. Magee, K. R. Seddon, and J. A. Widegren, "The distillation and volatility of ionic liquids," *Nature Letters*, vol. 439, pp. 831–834, February 2006.

[5] J. M. S. S. Esperanca, J. N. Canongia Lopes, M. Tariq, L. M. N. B. F. Santos, J. W. Magee, and L. P. N. Rebelo, "Volatility of Aprotic Ionic Liquids - A Review," *Journal of Chemical Engineering Data*, vol. 55, pp. 3–12, 2010.

[6] D. T. Sawyer, G. Chlericato, C. T. Angells, E. J. Nanni, and T. Tsuchlya, "Effects of Media and Electrode Materials on the Electrochemical Reduction of Dioxygen," *Analytical Chemistry*, vol. 54, no. number, pp. 1720–1724, 1982.

[7] J. A. Bautista-Martinez, L. Tang, J. P. Belieres, R. Zeller, and C. Friesen, "Hydrogen Redox in Protic Ionic Liquids and the Direct Extraction of Proton Energetics," *Journal of Physical Chemistry C*, vol. 113, pp. 12586–12593, 2009.

[8] *The Electrochemistry of Oxygen*. New York: John Wiley & Sons, Inc, 1968.

[9] *Electrochemical Oxygen Technology*. New York: John Wiley & Sons, Inc, 1992.

[10] *Electrocatalysis*. Wiley-VCH, 1998.

[11] *Handbook of Fuel Cells: Fundamentals, Technology and Applications*, ch. Oxygen Reduction Reaction on Smooth Single Crystal Electrodes. John Wiley and Sons, Ltd, 2003.

[12] N. A. Anastasijevic, V. Vesovic, and R. R. Adzic, "Determination of the Kinetic Parameters of the Oxygen Reduction Reaction Using the Rotating-Ring Disk Electrode. Part I: Theory," *Journal of Electroanalytical Chemistry*, vol. 229, pp. 305–316, 1987.

[13] N. A. Anastasijevic, V. Vesovic, and R. R. Adzic, "Determination of the Kinetic Parameters of the Oxygen Reduction Reaction Using the Rotating-Ring Disk Electrode. Part II: Applications," *Journal of Electroanalytical Chemistry*, vol. 229, pp. 317–325, 1987.

[14] B. B. Blizanac, P. N. Ross, and N. M. Markovic, "Oxygen electroreduction on Ag(111): The pH effect," *Electrochimica Acta*, vol. 52, no. number, pp. 2264–2271, 2007.

[15] S. Strbac, "The effct of pH on oxygen and hydrogen peroxide reduction on polycrystalline Pt electrode," *Electrochimica Acta*, vol. unkn, p. unkn, 2010.

[16] E. Yeager, "Dioxygen Electrocatalysis: Mechanisms in relation to Catalyst Structure," *Journal of Molecular Catalysis*, vol. 38, pp. 5–35, November 1986.

[17] T. J. Schmidt, M. Stamenkovic, N. M. Arenz, and P. N. Ross, "Oxygen electrocatalysis in alkaline electrolyte: Pt(hkl), Au(hkl) and the effect of Pd-modification," *Electrochimica Acta*, vol. 47, no. 22-23, pp. 3765–3776, 2002.

[18] V. Stamenkovic, T. J. Schmidt, P. N. Ross, and N. M. Markovic, "Surface Composition Effects in Electrocatalysis: Kinetics of Oxygen Reduction on Well-defined Pt3Ni and Pt3Co Alloy Surfaces," *Journal of Physical Chemistry B*, vol. 106, pp. 11970–11979, 2002.

[19] N. M. Markovic, R. R. Adzic, B. D. Cahan, and E. B. Yeager, "Structural effects in electocatalysis: oxygen reduction on platinum low index single-crystal surfaces in perchloric acid solutions," *Journal of Electroanalytical Chemistry*, vol. 377, pp. 249–259, 1994.

[20] N. M. Markovic, H. A. Gasteiger, and P. N. Ross, "Oxygen Reduction on Pt low-index single crystal surfaces in Sulfuric Acid Solution: RDE Pt(hkl) Disk Studies," *Journal of Physical Chemistry*, vol. 99, no. 11, pp. 3411–3415, 1995.

[21] R. W. Zurilla, R. K. Sen, and E. Yeager, "The Kinetics of the Oxygen Reduction Reaction on Gold in Alkaline Solution," *Journal of the Electrochemical Society*, vol. 125, pp. 1103–1109, July 1978.

[22] E. J. Taylor, N. R. K. Vilambi, and A. Gelb, "The Nature of the Catalytic Peak for Oxygen Reduction in Alkaline Electrolyte on the Au(100) Surface," *Journal of the Electrochemical Society*, vol. 136, p. 1939, July 1989.

[23] *Atlas of electrochemical equilibria in aqueous solutions*. Houston, Texas: National Association of Corrosion Engineers, 2 ed., 1974.

[24] L. Genies, Y. Bultel, R. Faure, and R. Durand, "Impedance study of the oxygen reduction reaction on platinum nanoparticles in alkaline media," *Electrochimica Acta*, vol. 48, pp. 3879–3890, 2003.

[25] R. Memming, "Mechanism of the Electrochemcial Reduction of Persulfates and Hydrogen Peroxide," *Journal of the Electrochemical Society: Electrochemical Science*, vol. 116, no. 6, pp. 785–790, 1969.

[26] A. J. Appleby and M. Savy, "Kinetics of Oxygen Reduction Reactions Involving Catalytic Decomposition of Hydrogen Peroxide: Application to Porous and Rotating Ring-Disk Electrodes," *Journal of Electroanalytical Chemistry*, vol. 92, pp. 15–30, 1978.

[27] F. van den Brink, E. Barendrecht, and W. Visscher, "Hydrogen peroxide as an Intermediate in Electrocatalytic Reduction of Oxygen. A New Method for the Determination of Rate Constants," *Electrochemical Science and Technology*, vol. 127, pp. 2003–2006, September 1980.

[28] M. Honda, T. Kodera, and H. Kita, "Electrochemical Behavior of H2O2 at Ag in HClO4 Aqueous Solution," *Electrochimica Acta*, vol. 31, no. 3, pp. 377–383, 1986.

[29] G. Flatgen, S. Wasle, M. Lubke, C. Eickes, G. Radhakrishnan, K. Doblhofer, and G. Ertl, "Autocatalytic mechanism of H2O2 reduction on Ag electrodes in acidic electrolyte: experiments and simulations," *Electrochimica Acta*, vol. 44, pp. 4499–4506, 1999.

[30] J. K. Norskov, J. Rossmeisl, A. Logadottir, L. Lindqvist, J. R. Kitchin, T. Bligaard, and H. Jonsson, "Origin of the Overpotential for Oxygen Reduction at a Fuel-Cell Cathode," *Journal of Physical Chemistry, B*, vol. 108, pp. 17886–17892, 2004.

[31] V. Tripkovic, E. Skulason, S. Siahrostami, J. K. Norskov, and J. Rossmeisl, "The oxygen reduction reaction mechanism on Pt(111) from density functional theory calculations," *Electrochimica Acta*, vol. 55, pp. 7975–7981, 2010.

[32] D. T. Sawyer and J. L. Roberts, "Electrochemistry of Oxygen and Superoxide Ion in Dimethylsulfoxide at Platinum, Gold and Mercury Electrodes," *Journal of Electroanalytical Chemistry*, vol. 12, pp. 90–101, 1966.

[33] C. Louis and R. L. Benoit, "The Electrochemical Reduction of Oxygen in Sulpholane," *Electrochimica Acta*, vol. 18, pp. 7–12, 1973.

[34] D. T. Sawyer and J. S. Valentine, "How Super is Superoxide?," *Accounts of Chemical Research*, vol. 14, no. number, pp. 393–400, 1981.

[35] D. Vasudevan and H. Wendt, "Electroreduction of Oxygen in Aprotic Media," *Journal of Electroanalytical Chemistry*, vol. 192, pp. 69–74, 1995.

[36] C. Costentin, D. H. Evans, M. Robert, J.-M. Saveant, and P. S. Singh, "Electrochemical Approach to the Concerted Proton and Electron Transfers. Reduction of the Water-Superoxide Ion Complex," *Journal of the American Chemical Society*, vol. 127, no. 36, pp. 12490–12491, 2005.

[37] P. S. Singh and D. H. Evans, "Study of the Electrochemical Reduction of Dioxygen in Acetonitrile in Presence of Weak Acids," *Journal of Physical Chemistry, B*, vol. 110, pp. 637–644, 2006.

[38] C. Villagran, L. Aldous, M. C. Lagunas, R. G. Compton, and C. Hardacre, "Electrochemistry of phenol in bis(trifluoromethyl)sulfonylamide ([NTf2]-) based ionic liquids," *Journal of Electroanalytical Chemistry*, vol. 588, pp. 27–31, 2006.

[39] A. Rene, D. Hauchard, C. Lagrost, and P. Hapiot, "Superoxide Protonation by Weak Acidsin Imidazolium Based Ionic Liquids," *Journal of Physical Chemistry, B*, vol. 113, no. 9, pp. 2826–2831, 2009.

[40] B. H. J. Bielski and D. E. Cabelli, "Highlights of current research involving superoxide and perhydroxyl radicals in aqeous solutions," *International Journal of Radiation Biology*, vol. 59, p. 291, 319 1991.

[41] K. E. Johnson, "What's and Ionic Liquid?," *Interface*, vol. 16, no. 1, pp. 38–41, 2007.

[42] R. E. Davis, G. L. Horvath, and C. W. Tobias, "Solubility and Diffusion Coefficient of Oxygen in Potassium Hydroxide Solutions," *Electrochimica Acta*, vol. 12, pp. 287–297, 1967.

[43] *Handbook of Chemistry and Physics*. CRC Press, 85 ed., 2004-2005.

[44] J. Jordan, E. Ackerman, and R. L. Berger, "Polarographic Diffusion Coefficients of Oxygen," *Journal of the American Chemical Society*, vol. 78, pp. 2979–2983, July 1956.

[45] R. N. Itoe, G. D. Wesson, and E. E. Kalu, "Evaluation of Oxygen Transport Parameters in Sulfuric Acid Methanol Mixtures Using Electrochemical Methods," *Journal of the Electrochemical Society*, vol. 147, no. 7, pp. 2445–2450, 2000.

[46] M. Tsushima, K. Tokuda, and T. Oshaka, "Use of Hydrodynamic Chronocoulometry for Simultaneous Determination of Diffusion Coefficients and Concentrations of Dioxygen in Various Media," *Analytical Chemistry*, vol. 66, pp. 4551–4556, 1994.

[47] J. M. Achord and C. L. Hussey, "Determination of Dissolved Oxygen in Nonaqeous Electrochemical Solvents," *Analytical Chemistry*, vol. 52, pp. 601–602, 1980.

[48] X.-J. Huang, E. I. Rogers, C. Hardacre, and R. G. Compton, "The Reduction of Oxygen in Various Room Temperature Ionic Liquids in the Temperature Range 293-318K: Exploring the Applicability of the Stokes-Einstein Relationship in Room Temperature Ionic Liquids," *Journal of Physical Chemistry B*, vol. 113, pp. 8953–8959, 2009.

[49] R. G. Evans, O. V. Klymenko, S. A. Saddaughi, C. Hardacre, and R. G. Compton, "Electroreduction of Oxygen in a Series of Room Temperature Ionic Liquids Composed of Group 15-Centered Cations and Anions," *Journal of Physical Chemistry B*, vol. 108, pp. 7878–7886, 2004.

[50] Y. Katayama, K. Sekiguchi, M. Yamagata, and T. Miura, "Electrochemical Behavior of Oxygen/Superoxide Ion Couple in 1-Butyl-1-methylpyrrolidinium Bis(trifluoromethylsulfonyl)imide Room-Temperature Molten Salt," *Journal of the Electrochemical Society*, vol. 152, no. 8, pp. E247–E250, 2005.

[51] D. R. MacFarlane, P. Meakin, J. Sun, N. Amini, and M. Forsyth, "Pyrrolidinium Imides: A New Family of Molten Salts and Conductive Plastic Crystal Phases," *Journal of Physical Chemistry, B*, vol. 103, no. 20, pp. 4164–4170, 1999.

[52] M. Shamsipur, A. A. M. Beigi, M. Teymouri, S. M. Pourmortazavi, and M. Irandoust, "Physical and Electrochemical Properties of Ionic Liquids 1-ethyl-3-methylimidazolium tetrafluoroborate, 1-butyl-3-methylimidazolium trifluoromethanesulfonate and 1-butyl-3-methylimidazolium bis(trifluoromethylsulfonyl)imide," *Journal of Molecular Liquids*, vol. 157, pp. 43–50, 2010.

[53] T. J. VanderNoot and O. O. Okoturo, "Temperature dependence of Viscosity for room temperature ionic liquids," *Journal of Electroanalytical Chemistry*, vol. 568, pp. 167–181, July 2004.

[54] C. Buzzeo, Marisa, C. Hardacre, and R. G. Compton, "Use of Room Temperature Ionic Liquids in Gas Sensor Design," *Analytical Chemistry*, vol. 76, pp. 4583–4588, 2004.

[55] A. S. Barnes, E. I. Rogers, I. Streeter, L. Aldous, C. Hardacre, G. G. Wildgoose, and R. G. Compton, "Unusual Voltammetry of the Reduction of O2 in [C4dmim][N(Tf)2] Reveals a Strong Interaction of Superoxide with the [C4dmim]+ Cation," *Journal of Physical Chemistry*, vol. 112, pp. 13709–13715, 2008.

[56] J. Ghilane, C. Lagrost, and P. Hapiot, "Scanning Electrochemical Microscopy in Nonusual Solvents: Inequality of Diffusion Coefficients Problem," *Analytical Chemistry*, vol. 79, pp. 7383–7391, 2007.

[57] P. Bonhote, A.-P. Dias, N. Papageorgiou, K. Kalyanasundaram, and M. Gratzel, "Hydrophobic, Highly Conductive Ambient-Temperature Molten Salts," *Inorganic Chemistry*, vol. 35, pp. 1168–1178, 1996.

[58] C. Han, G. Yu, L. Wen, C. Asumana, and X. Chen, "Data and QSPR study for viscosity imidazolium-based ionic liquids," *Fluid Phase Equilibria*, vol. 300, pp. 95–104, January 2011.

[59] M. Yoshizawa, W. Xu, and C. A. Angell, "Ionic Liquids by Proton Transfer: Vapor Pressure, Conductivity, and Relevance of dpKa from Aqueous Solutions," *Journal of the American Chemical Society*, vol. 125, pp. 15411–15419, 2003.

[60] J.-P. Belieres and C. A. Angell, "Protic Ionic Liquids: Preparation, Characterization and Proton Free Energy Level Representation," *Journal of Physical Chemistry, B*, vol. 111, pp. 4926–4937, 2007.

[61] L. Tang, J. A. Bautista-Martinez, L. Mickelson, R. Zeller, J. P. Belieres, C. A. Angell, and C. Friesen, "Oxygen Reduction in Protic Ionic Liquds." in progress.

[62] D. Zhang, T. Okajima, F. Matsumoto, and T. Ohsaka, "Electroreduction of Dioxygen in 1-n-Alkyl-3-methylimidazolium Tetrafluoroborate Room-Temperature Ionic Liquids," *Journal of the Electrochemical Society*, vol. 151, no. 4, pp. D31–D37, 2004.

[63] M. M. Islam, B. N. Ferdousi, T. Okajima, and T. Oshaka, "A catalytic avtivity of mercury electrode towards dioxygen reduction in room-temperature ionic liquids," *Electrochemistry Communications*, vol. 7, pp. 789–795, 2005.

[64] S. Millefiorini, A. H. Tkaczyk, R. Sedev, J. Efthimiadis, and J. Ralston, "Electrowetting of Ionic Liquids," *Journal of the American Chemical Society*, vol. 128, pp. 3098–3101, 2006.

[65] J. Restolho, J. L. Mata, and B. Saramago, "Electrowetting of Ionic Liquids: Contact Angle Saturation and Irreversibility," *Journal of Physical Chemistry, C*, vol. 113, pp. 9321–9327, 2009.

[66] P. M. Gouy, "Sur la constitution de la charge lectrique la surface d'un lectrolyte," *Journal de Physique Thorique et Applique*, vol. 9, pp. 457–468, June 1910.

[67] D. L. Chapman, "A contribution to the theory of electrocapillarity," *Philosophical Magazine*, vol. 25, no. 148, pp. 475–481, 1913.

[68] O. Z. Stern, "The theory of the electrolytic double-layer.," *Zeitschrift fur Elektrochemie und Angewandte Physikalische Chemie*, vol. 30, pp. 508–516, 1924.

[69] D. C. Grahame, "The Electrical Double Layer and the Theory of Electrocapillarity.," *Chemical Reviews*, vol. 41, pp. 441–501, December 1947.

[70] *Analytical and Physical Electrochemistry*. EPFL Press, 2004.

[71] V. Lockett, M. Horne, R. Sedev, T. Todopoulos, and J. Ralston, "Differential Capacitance of the double layer at the electrode/ionic liquids interface," *Phsyical Chemistry Chemical Physics*, vol. 12, pp. 12499–12512, 2010.

[72] A. A. Kornyshev, "Double-Layer in Ionic Liquids: Paradigm Change?," *Journal of Physical Chemistry, B*, vol. 111, pp. 5545–5557, 2007.

[73] K. B. Oldham, "A Gouy-Chapman-Stern model of the double layer at a (metal)/(ionic liquid) interface," *Journal of Electroanalytical Chemistry*, vol. 613, pp. 131–138, 2008.

[74] V. Lockett, R. Sedev, J. Ralston, M. Horne, and T. Rodopoulos, "Differential Capacitance of the Electrical Double Layer in Imidazolium-Based Ionic Liquids: Influence of Potential, Cation Size, and Temperature," *Journal of Physical Chemistry, C*, 2008.

[75] Y. Lauw, M. D. Horne, T. Rodopaulos, and F. A. M. Leermakers, "Room-Temperature Ionic Liquids: Excluded Volume and Ion Polarizability Effects in the Electrical Double-Layer Structure and Capacitance," *Phsyical Review Letters*, vol. 103, pp. 1–4, September 2009.

[76] Y. Lauw, M. D. Horne, T. Rodopoulos, and F. A. M. Leermakers, "Electrical Double-Layer Capacitance in Room Temperature Ionic Liquids: Ion-Size and Specific Adsorption Effects," *Journal of Phsyical Chemistry, B*, 2010.

[77] M. V. Fedorov, N. Georgi, and A. A. Kornyshev, "Double layer in ionic liquids: The nature of the camel shape of capacitance," *Electrochemistry Communications*, vol. 12, pp. 296–299, 2010.

[78] M. Z. Bazant, B. D. Storey, and A. A. Kornyshev, "Double Layer in Ionic Liquids: Overscreening versus Crowding," *Physical Review Letters*, vol. 106, p. 046102, Nanuary 2011.

[79] R. Hayes, N. Borisenko, M. K. Tam, P. C. Howlett, F. Endres, and R. Atkin, "Double Layer Structure of Ionic Liquids at the Au(111) Electrode Interface: An Atomic Force Microscopy Investigation," *Journal of Physical Chemsitry, C*, vol. 115, pp. 6855–6863, 2011.

[80] R. J. Gale and R. A. Osteryoung, "The electrical double layer at mercury in room temperature aluminum chloride: 1-butylpyridinium chloride ionic liquids," *Electrochimica Acta*, vol. 25, pp. 1527–1529, 1980.

[81] E. A. Ukshe, N. G. Bukun, D. I. Leikis, and A. N. Frumkin, "Investigation of the Electric Double Layer in Salt Melts," *Electrochimica Acta*, vol. 9, pp. 431–439, month 1964.

[82] A. D. Graves and D. Inman, "The electrical double layer in molten salts: Part 1. the potential of zero charge," *Electroanalytical Chemistry and Interfacial Electrochemistry*, vol. 25, pp. 349–356, 1970.

[83] A. D. Graves and D. Inman, "The electrical double layer in molten salts: Part 2. the double-layer capacitance," *Electroanalytical Chemistry and Interfacial Electrochemistry*, vol. 25, pp. 357–372, 1970.

[84] C. Nanjundiah, S. F. McDevitt, and V. R. Koch, "Differential capacitance measurements in solvent-free ionic liquids at hg and c interfaces," *Journal of the Electrochemical Society*, vol. 144, pp. 3392–3397, October 1997.

[85] F. H. Stillinger and J. G. Kirkwood, "Theory of the Diffuse Double Layer," *Journal of Chemical Physics*, vol. 33, pp. 1282–1290, November 1960.

[86] F. Silva, C. Gomes, M. Figueiredo, R. Costa, A. Martins, and C. M. Pereira, "The electrical double at the [BMIM][PF6] ionic liquid/electrode interface - Effect of temperature on the differential capacitance," *Journal of Electroanalytical Chemistry*, vol. 622, pp. 153–160, 2008.

[87] *Electrochemistry*. Weinheim, Germany: Wiley-VCH, 1 ed., 1998.

[88] S. Bruckenstein and G. A. Feldman, "Radial Transport Times at Rotating Ring-Disk Electrodes. Limitations on the Detection of Electrode Intermediates Ungergoing Homogeneous Chemical Reactions," *Journal of Electroanalytical Chemistry*, vol. 9, no. 5-6, pp. 395–399, 1965.

[89] D. Shoup and A. Szabo, "Chronoamperometric Current at Finite Disk Electrodes," *Journal of Electroanalytical Chemistry*, vol. 140, pp. 237–245, 1982.

[90] G. S. Alberts and I. Shain, "Electrochemical Study of Kinetics of a Chemical Reaction Couple Between Twho Charge Transfer Reactions," *Analytical Chemistry*, vol. 35, no. 12, pp. 1859–1866, 1963.

[91] T. Pajkossy, "Impedance of rough capacitive electrodes," *Journal of Electroanalytical Chemistry*, vol. 634, pp. 111–125, 1994.

[92] W. Xu and C. A. Angell, "Solvent-free electrolytes with aqueous solution-like conductivities," *Science*, vol. 302, no. 5644, pp. 422–425, 2003.

[93] H. Nakamoto, A. Noda, K. Hayamizu, S. Hayashi, H.-o. Hamaguchi, and M. Watanabe, "Proton-conducting Properties of a bronsted acid-base ionic liquid and ionic melts consisting of bis(trifluoromethansulfonyl)imide and benzimidazole for fuel cell electrolytes," *Journal of Physical Chemistry C*, vol. 111, no. 3, pp. 1541–1548, 2007.

[94] H. Nakamoto and M. Watanabe, "Bronsted acid-base ionic liquids for fuel cell electrolytes," *Chemical Communications*, vol. 24, no. number, pp. 2539–2541, 2007.

[95] J. P. Belieres, D. Gervasio, and C. A. Angell, "Binary inorganic salt mixtures as high conductivity liquid electrolytes for 100C+ fuel cells," *Chemical Communications*, vol. 46, pp. 4799–4801, 2006.

[96] T. Robert, L. Magna, H. Olivier-Bourbigou, and B. Gilbert, "A comparison of the Acidity Levels in Room-Temperature Ionic Liquids," *Journal of The Electrochemical Society*, vol. 156, no. 9, pp. F115–F121, 2009.

[97] M. C. Buzzeo, O. V. Klymenko, J. D. Wadhawan, C. Hardacre, K. R. Seddon, and R. G. Compton, "Voltammetry of Oxygen in the Room-Temperature Ionic Liquids 1-ethyl-3-methylimidaozlium bis((trifluoromethyl)sulfonyl)imide and hexyltriethylammonium bis((trifluoromethyl)sulfonyl)imide: One-Electron Reduction to Form Superoxide. Steady-State and Transient Behavior in the same Cyclic Voltammogram Resulting from Widely Different Diffusion Coefficients of Oxygen and Superoxide," *Journal of Physical Chemistry A*, vol. 107, pp. 8872–878, 2003.

[98] Y. Katayama, H. Onodera, M. Yamagata, and T. Miura, "Electrochemical Reduction of Oxygen in Some Hydrophobic Room-Temperature Molten Salt Systems," *Journal of the Electrochemical Society*, vol. 151, no. 1, pp. A59–A63, 2004.

[99] C. L. Brosseau, E. Sheepwash, I. J. Burgess, E. Cholewa, S. G. Roscoe, and J. Lipkowski, "Adsorption of N-Decyl-N,N,N-trimethylammonium Triflate (DeTATf), a Cationic Surfactant, on the Au(111) Electrode Surface," *Langmuir*, vol. 23, pp. 1784–1791, 2007.

[100] M. M. Islam, T. Imase, T. Okajima, M. Takahashi, Y. Niikura, N. Kawashima, Y. Nakamura, and T. Oshaka, "Stability of Superoxide Ion

in Imidazolium Cation-Based Room-Temperature Ionic Liquids," *Journal of Physical Chemistry, A*, vol. 113, no. 5, pp. 912–916, 2009.

[101] M. M. Islam and T. Oshaka, "Two-electron quasi-reversible reduction of dioxygen at HDME in ionic liquids: Observation of cathodic maximum and inverted peak," *Journal of Electroanalytical Chemistry*, vol. 623, pp. 147–154, 2008.

[102] P. C. Trulove, D. K. Sukumaran, and R. A. Osteryoung, "Protons in Acidic ambient-Temperature Chloroaluminate Molten Salts: Hydrogen-Deuterium Exchange between the Imidazolium Cation and Hydrogen Chloride," *Journal of Physical Chemistry*, vol. 98, no. 1, pp. 141–146, 1994.

[103] D. H. Ripin and D. A. Evans, "pKa's of Inorganic and Oxo-Acids," January 2011.

[104] T. Rodima, I. Kaljurand, A. Pihl, V. Maemets, I. Leito, and I. Koppel, "Acid-Base Equilibria in Nonpolar Media. 2. Self-Consistent Basicity Scale in THF Solution Ranging from 2-Methoxyypyridine to EtP1(pyrr) Phosphazene," *Journal of Organic Chemistry*, vol. 67, pp. 1873–1881, 2002.

[105] T. Robert, L. Magna, H. Oliver-Bourbigou, and B. Gilbert, "A Comparison of the Acidity Levels in Room-Temperature Ionic Liquids," *Journal of The Electrochemical Society*, vol. 156, no. 9, pp. F115–F121, 2009.

[106] J. S. Wilkes and M. J. Zaworotko, "Air and water stable 1-ethyl-3-methylimidazolium based ionic liquids," *Journal of the Chemical Society. Chemical communications*, 1992.

[107] R. G. Pearson, "Hard and soft acids and bases," *Journal of the American Chemical Society*, vol. 85, pp. 3533–3539, November 1963.

[108] L. Cammarata, S. G. Kazarian, P. A. Salter, and T. Welton, "Molecular states of water in room temperature ionic liquids," *Pysical Chemistry Chemical Physics*, vol. 3, pp. 5192–5200, 2001.

[109] J. L. Anthony, E. J. Maginn, and J. F. Brennecke, "Solution thermodynamics of imidazolium-based ionic liquids and water," *Journal of Physical Chemistry*, 2001.

[110] L. Landau and B. Levich, "Dragging of a Liquid by a Moving Plate," *Acta Physicochimica U.R.S.S.*, vol. 27, no. 1-2, pp. 1542–1554, 1944.

[111] W. Jiang, Y. Wang, and G. A. Voth, "Molecular Dynamics Simulation of Nanostructural Organization in Ionic Liquid/Water Mixtures," *Journal of Physical Chemistry, B*, vol. 111, pp. 4812–4818, 2007.

[112] S. T. Handy and M. Okello, "The 2-Position of Imidazolium Ionic Liquids: Substitution and Exchange," *Journal of Organic Chemistry*, vol. 70, pp. 1915–1918, 2005.

[113] P. Cofre and D. T. Sawyer, "Electrochemical Reduction of Dioxygen to Perhydroxyl (HO2*) in Aprotic Solvents That Contain Bronsted Acids," *Analytical Chemistry*, vol. 58, pp. 1057–1062, 1986.